Earth System
Science
Data

Open Access

Supplement of

Global nitrous oxide budget (1980–2020)

Hanqin Tian et al.

Correspondence to: Hanqin Tian (hanqin.tian@bc.edu)

1   **Extended methodology**
2
3   **S1.1 NMIP-2**: global **N**itrogen/N$_2$O **M**odel **I**nter-comparison **P**roject phase **2**
4
5   The NMIP2 is a follow-up model intercomparison project of NMIP (*Tian et al.*, 2018), which provides
6   estimates of N$_2$O emissions from natural and agricultural soils and covers the time period 1850-2020. Eight
7   process-based Terrestrial Biosphere Models (TBMs) participate in NMIP-2. In general, N$_2$O emissions
8   from soil are regulated at two levels, which are the rates of nitrification and denitrification in the soil and
9   soil physical factors regulating the ratio of N$_2$O to other nitrous gases (*Davidson et al.*, 2000). For N input
10 to land ecosystems, all eight models considered N fertilizer use, atmospheric N deposition and biological
11 fixation, but five models considered manure as N input. For vegetation processes, all models included
12 dynamic algorithms in simulating N allocation to different living tissues and vegetation N turnover, and
13 simulated plant N uptake using the "Demand and Supply-driven" approach. For soil N processes, all eight
14 models simulated N leaching according to water runoff rate; however, models are different in representing
15 nitrification and denitrification processes and the impacts of soil chemical and physical factors. The
16 differences in simulating nitrification and denitrification processes are one of the major uncertainties in
17 estimating N$_2$O emissions. Model characteristics in simulating major N cycling processes associated with
18 N$_2$O emissions in each participating model are briefly described in Table S1.
19
20 **Table S1. Model characteristics in simulating major N cycling processes**

	CLASS IC	DLEM	ELM	ISAM	LPX-Bern	O-CN	ORCHIDEE	VISIT
Open C cycle [a]	Yes	Yes	Yes	Yes	Yes	Yes	Yes	Yes
C-N coupling	Yes	Yes	Yes	Yes	Yes	Yes	Yes	Yes
N pools [b]	(3, 1, 3)	(6,6,8)	(6,4,5)	(6,4,4)	(4,3,8)	(9,6,9)	(9,6,9)	(4,1,4)
Demand and supply–driven plant N uptake	Yes	Yes	Yes	Yes	Yes	Yes	Yes	Yes
N allocation [c]	Dynamic	Dynamic	Dynamic	Dynamic	Dynamic	Dynamic	Dynamic	Dynamic
Nitrification	$f(T, SWC, C_{NH4})$	$f(T, SWC, C_{NH4})$	$f(T, SWC, pH, rh, C_{NH4})$	$f(T, SWC, C_{NH4})$	$f(T, SWC, C_{NH4})$	$f(T, SWC, pH, C_{NH4})$	$f(T, SWC, pH, C_{NH4})$	$f(T, SWC, pH, C_{NH4})$
Denitrification	$f(T, SWC, C_{NO3})$	$f(T, SWC, clay, rh, C_{NO3})$	$f(T, SWC, pH, rh, C_{NO3})$	$f(T, SWC, C_{NO3})$	$f(T, SWC, R_{mb}, C_{NO3})$	$f(T, SWC, pH, R_{mb}, C_{NO3})$	$f(T, SWC, pH, denitrifier, C_{NO3})$	$f(SWC, rh, C_{NO3})$
Mineralization, immobilization	$f(C{:}N)$	$f(C{:}N)$	$f(C{:}N)$	$f(C{:}N)$	$f(C{:}N)$	$f(C{:}N)$	$f(C{:}N)$	$f(C{:}N)$
N leaching	$f(runoff, C_{NO3}, C_{NH4})$	$f(runoff, C_{NO3}, C_{NH4})$	$f(runoff, C_{NO3})$	$f(runoff, C_{NO3}, C_{NH4})$	$f(runoff, C_{NO3})$	$f(runoff, C_{NO3}, C_{NH4})$	$f(runoff, C_{NO3}, C_{NH4})$	$f(runoff, C_{NO3})$
NH$_3$ volatilization	$f(C_{NH3})$	$f(T, SWC,$	No	$f(C_{NH3})$	$f(T, SWC,$	$f(C_{NH3})$	$f(SWC, pH, C_{NH4})$	$f(T, SWC,$

		pH, C_{NH4})			pH, C_{NH4})			pH, C_{NH4})
Plant N turnover [d]	Dynamic	Dynamic	Dynamic	Dynamic	Dynamic	Dynamic	Dynamic	Dynamic
N resorption	Fixed	f(C:N)	Fixed	f(C:N)	Fixed	Fixed	Fixed	Fixed
N fixation	f(N_{limit})	f(T, SWC, C_{NH4}, C_{NO3})	f(T, C:N)	f(ET)	Implied by mass balance	f(N_{limit})	Fixed	f(ET)
N fertilizer use	Yes	Yes	Yes	Yes	Yes	Yes	Yes	Yes
Manure N use	No	Yes	No	Yes	No	Yes	Yes	Yes
N deposition	Yes	Yes	Yes	Yes	Yes	Yes	Yes	Yes

[a] "Open" denotes that excess N can be leached from the system.
[b] Numbers of N pools (vegetation pools, litter pools, soil pools).
[c] Dynamic denotes time-varied N allocation ratio to different N pools.
T: soil temperature, SWC: soil water content, clay: soil clay fraction, ET: evapotranspiration, denitrifier:
soil denitrifier biomass, rh: soil heterogeneous respiration, Nlimit: N limitation of vegetation growth,
C_{NO3}: soil NO_3^- content, C_{NH4}: soil NH_4^+ content.

All NMIP2 models are driven by consistent input datasets (i.e., climate, atmospheric CO_2 concentration, land cover change, irrigation, atmospheric N deposition, mineral N fertilization, and manure N application and deposition) and implemented consistent simulation experiments (SH0 – SH12; Table A4). Nitrogen inputs data used in NMIP2 simulations are from History of anthropogenic Nitrogen inputs (HaNi) dataset (*Tian et al.*, 2022), which takes advantage of different data sources in a spatiotemporally consistent way to generate a set of high-resolution (5 arcminutes) gridded N input products from 1850 to 2020. HaNi data set shows that the total anthropogenic N inputs to global terrestrial ecosystems increased from 29.05 Tg N yr^{-1} in the 1860s to 267.23 Tg N yr^{-1} in the 2010s, with the dominant N source changing from atmospheric N deposition (before the 1900s) to manure N (the 1910s-2000s), and to synthetic fertilizer in the 2010s (Fig. B3). The climate data used to run historical simulations is the half degree CRU-JRA2.2 6-hourly forcing over 1901- 2020 (https://catalogue.ceda.ac.uk/uuid/4bdf41fc10af4caaa489b14745c665a6). Annual CO_2 concentration during 1850-2020 were derived from ice core CO_2 data and NOAA annual observations(https://www.esrl.noaa.gov). Historical distribution of cropland, pasture, rangeland and irrigation during 1850-2020 were from Land-Use Harmonization 2 (LUH2) dataset (*Hurtt et al.*, 2020). The original dataset of LUH2 is at a resolution of 0.25° x 0.25° longitude/latitude. We aggregated all geo-referenced input data into a consistent spatial resolution of 0.5° x 0.5° longitude/latitude to run NMIP2 models.

NMIP2 models perform a subset of 13 simulations (SH0-SH12) to quantify N_2O emissions from both agricultural and natural soils during the study period, and to disentangle the effects of multiple environmental factors on soil N_2O emissions. The SH1 results were taken as the "best estimates" of soil N_2O emissions because they include the effects of all driving factors that models can take into account. In the SH0 simulation, driving forces were kept constant at the level in 1850 over the entire simulation period (1850-2020). According to previous N_2O budget studies, atmospheric N_2O growth rate and Monte-Carlo method, we suggest the following criteria for the N_2O budget inclusion (Table A6), and the criteria for carbon components are consistent with TRENDY. By comparing results from factorial simulation experiments (SH0 - SH12), we attribute changes in soil N_2O emissions to seven natural and anthropogenic factors, namely, climate (CLIM, including precipitation, humidity, temperature and photosynthetic active radiation changes), atmospheric CO_2 concentration (CO_2), land cover change (LCC), irrigation (IRRI),

57 atmospheric N deposition (NDEP), mineral N fertilizer use (NFER), and manure N use in cropland
58 (MANN). In order to understand soil N_2O emissions dynamics caused by crop cultivation, we further
59 separate the global and regional N_2O emissions into those derived from cropland soils and those from soils
60 of other land ecosystems. In this study, we attribute the impact of a single factor on cropland N_2O emissions.
61 Five models (DLEM, ISAM, O-CN, ORCHIDEE, and VISIT) considered the effects of manure N
62 application in cropland, therefore, we use these five models' results to calculate the manure N effect (SH1-
63 SH2). Meanwhile, we used results from all the eight models (i.e., CLASSIC, DLEM, ELM, ISAM, LPX-
64 Bern, O-CN, ORCHIDEE, and VISIT) to calculate the effects of synthetic N fertilizer use (SH1-SH3) and
65 atmospheric N deposition (SH1-SH4). The effect of N deposition in natural ecosystems (SH1-SH4) and the
66 effects of CO_2 (SH1-SH7) and climate (SH1-SH8) on global terrestrial ecosystems are calculated from the
67 eight NMIP2 models mentioned above.
68
69 **Table S2. Criteria for the N_2O budget inclusion**

Carbon criteria	N_2O criteria
(1) Steady state after spin-up, diagnosed from SH0 run: steady-state defined as an offset < 0.10 PgC yr^{-1}, drift < 0.05 PgC yr^{-1} per century (i.e. first is the average over 1850-2020, second is the slope x 100).	(1) Steady state after spin-up, diagnosed from SH0 run: drift < 0.2 Tg N_2O-N yr^{-1} per century (i.e. the slope x 100).
(2) Net annual land flux is a carbon sink over the 1990s and 2000s as constrained by global atmospheric and oceanic observations (Keeling & Manning, 2014), diagnosed from SH3 run.	(2) Inside the present-day (2007-2016) land emission range: 7-13 Tg N_2O-N yr^{-1}, diagnosed from SH1 run. The upper limit was calculated using the maximum total N_2O emissions minus the minimum estimates of other sources, and the lower limit was calculated using the minimum total N_2O emissions minus the maximum estimates of other sources. The range of total emissions was estimated by a one-box model using atmospheric N_2O growth rate, and the range of the sum of other sources was calculated by a Monte-Carlo method using estimates from Tian et al. (2020).
	(3) Inside the pre-industrial land emission range: 3 to 9 Tg N_2O-N yr^{-1}, diagnosed from SH1 run. This range is derived from the pre-industrial atmospheric burden/N_2O lifetime minus ocean and river/ coastal/estuary emissions (Michael J. Prather et al., 2015).

70
71
72 **S1.2 Brief description of algorithms associated with N_2O flux in each NMIP2 model:**

73 **S1.2.1: CLASSIC**

74 The representation of nitrogen cycling in CLASSIC is described in *Asaadi and Arora* (2021) and *Kou*
75 *Giesbrecht and Arora* (2022). N_2O production due to both nitrification and denitrification are represented.
76 N_2O loss during nitrification (I_{N_2O}; g N m^{-2} d^{-1}) is represented with the following equation:
77      $I_{N_2O} = \eta_{N_2O} f_I(T_{0.5}) f_I(\psi) N_{NH_4}$ (1)
78 η_{N_2O} is a coefficient (d^{-1}), $f_I(T_{0.5})$ is a dimensionless scalar that depends on soil temperature averaged over
79 the top 0.5m soil depth ($T_{0.5}$), $f_I(\psi)$ is a dimensionless scalar that depends on soil matric potential (ψ), and
80 N_{NH_4} is the soil ammonium pool (g N m^{-2}).
81 N_2O loss during denitrification (E_{N_2O}; g N m^{-2} d^{-1}) is represented with the following equation:

82 $$E_{N_2O} = \mu_{N_2O} f_E(T_{0.5}) f_E(\theta) N_{NO_3} \tag{2}$$

83 μ_{N_2O} is a coefficient (d⁻¹), $f_E(T_{0.5})$ is a dimensionless scalar that depends on soil temperature averaged over
84 the top 0.5m soil depth ($T_{0.5}$), $f_E(\theta)$ is a dimensionless scalar that depends on soil moisture (θ), and N_{NO_3}
85 is the soil nitrate pool (g N m⁻²).

86

87 **S1.2.2: DLEM**

88 The nitrogen cycle scheme in DLEM2.0 (*Xu et al.*, 2017; *Yang et al.*, 2015; Tian et al. 2020) are similar as
89 DLEM1.0 (*Lu and Tian*, 2013; *Tian et al.*, 2012b; *Tian et al.*, 2010; *Tian et al.*, 2011; *Xu et al.*, 2011),
90 However, the N₂O emission schemes in DLEM2.0 (*Xu et al.*, 2017) have been modified based on *Chatskikh*
91 *et al.* (2005) and *Heinen* (2006).

92

93 $$R_{nit} = k_{nit\_max} f(T1) f(WFPS) C_{NH4} \tag{3}$$

94

95 $$R_{den} = k_{den\_max} f(T2) f(WFPS) C_{NO3} \tag{4}$$

96

97 where R_{nit} is the daily nitrification rate (g N/m²/d); R_{den} is the daily denitrification rate (g N/m²/d);
98 $f(T1)$ and $f(T2)$ are the impact function of daily soil temperature on nitrification and denitrification,
99 respectively; $f(WFPS)$ is the impact function of water-filled pore space (WFPS) on nitrification,
100 denitrification and N₂O diffusion; k_{nit_max} is the maximum fraction of NH₄⁺-N that is converted to NO₃⁻-
101 N or gases (0-1); k_{den_max} is the maximum fraction of NO₃⁻-N that is converted to gases (0-1); C_{NH4} and
102 C_{NO3} are the soil NH₄⁺-N and NO₃⁻-N content (g N/m²). N₂O from denitrification and nitrification processes
103 are calculated as,

104

105 $$R_{N2O} = (R_{nit} + R_{den}) f(T3)(1 - f(WFPS)) \tag{5}$$

106

107 where R_{N2O} is the daily N₂O emission rate (g N/m²/d); $f(T3)$ is the impact function of daily soil
108 temperature on N₂O diffusion rate from soil pores. The calculation methods for these functions and
109 parameters were described in detail in *Xu et al.* (2017) and *Yang et al.* (2015).

110

111 **S1.2.3: ELM**

112 The nitrogen dynamics in ELM is simulated based on the theory of equilibrium chemistry approximation
113 (*Zhu et al.*, 2016). Plants, soil microbes, and abiotic factors such as mineral surfaces coexist in the same
114 soil environment and vie for a diverse array of nutrients, including NH4+, NO3-. Due to the limited
115 availability of these nutrients, intense competitive interactions are expected. The competition of those
116 limited resources is represented by consumer–substrate networks, therefore, the uptake of nutrient substrate
117 by each consumer is dependent on the relative competitiveness of one consumer over the others. Nutrient
118 consumers' competitiveness is parametrized with kinetic parameters (Zhu et al., 2016). As a result, neither
119 plan nor soil microbes get the first priority to access nutrient substrates. Instead, when the potential nutrient
120 demands (from all nutrient consumers) exceed the supply at a given time step, the allocation of limited
121 nutrients among the consumers affects their performance (e.g., plant growth, soil organic matter
122 accumulation, nitrification, denitrification rates). ELM adopts a multiple-consumer-multiple-substrate
123 competition network (Zhu et al., 2016; Zhu et al., 2019) to simulate (1) nitrogen uptake facilitated by
124 nitrogen carrier enzymes, (2) binding of a nutrient substrate to a particular enzyme precludes it from
125 attaching to other enzymes, and (3) rates and affinities of consumers for different substrates. After the
126 nutrient competition has been resolved, scaling terms ($f(ECA_{nit})$ and $f(ECA_{den})$) will be applied to the
127 potential nitrification and denitrification processes:

128

129 $$R_{nit} = k_{nit\_max} f(\theta) f(T)(1 - f(O)) f(ECA_{nit}) C_{NH4} \tag{6}$$

130

131    $R_{den} = min\,(f(deomp), f(C_{NO3}))f(ECA_{den})$ (7)

132

133   where k_{nit_max} is the maximum nitrification rate, $f(\theta)$, $f(T)$, $f(O)$ are soil moisture, temperature, and
134   oxygen scalars, respectively. $f(deomp)$ and $f(C_{NO3})$ are carbon limited and NO3- limited denitrification
135   rates (*Del Grosso et al.*, 2000).

136

137   **S1.2.4: ISAM**

138   ISAM model contains detailed calculations of the terrestrial ecosystem's organic and mineral N cycle (*Yang*
139   *et al.*, 2009). The major N processes in ISAM include biological fixation, leaching, mineralization and
140   immobilization, plant uptake, nitrification, and denitrification. The soil biogeochemistry module of ISAM
141   shares the same ten soil layers (to 3.5 m depth) as the soil biogeophysics and calculates the vertical transport
142   of SOC and N (*Shu et al.*, 2020; *Yang et al.*, 2009). N_2O emission in ISAM N_2O is produced as a byproduct
143   of nitrification and denitrification (*Xu et al.*, 2021). N_2O module explicitly accounts for the vertical transport
144   of C, N, and O_2 within every soil layer for both saturated and unsaturated soil conditions by accounting for
145   the process of oxygen diffusing into the soil from the atmosphere and the soil oxygen supply. The model
146   also explicitly accounts for the effects of anoxic and oxic environments on nitrification (N_{ni}, Eq. 6) and
147   denitrification (N_{de}, Eq. 7). Both environments are calculated based on the fraction of anoxic soil depending
148   on soil O_2 concentration, which is non-linearly correlated with the chemical pathways forming N_2O.

149

150    $N_{ni} = NH_4^+ \times (1 - e^{-F_{te\_m} \times F_{sm\_m} \times r_{ni}}) \times F_{pH\_m\_ni} \times R_d$ (8)

151

152    $N_{de} = NO_3^- \times r_{de} \times Rh \times F_{pH\_m\_de} \times R_d$ (9)

153

154   where NH_4^+ and NO_3^- are ammonium and nitrate pool sizes; F_{te_m} is temperature modifier; F_{sm_m} is soil
155   moisture modifier; r_{ni} and r_{de} are base nitrification and denitrification rates; $F_{pH\_m\_ni}$ and $F_{pH\_m\_de}$ are pH
156   modifiers for nitrification and denitrification; R_d is relative soil anoxic fraction; Rh ($= 1 - R_d$) is heterotrophic
157   respiration.

158

159   Under anoxic soil conditions, N_2O is produced through denitrification, while under oxic soil conditions,
160   more N_2O is produced from nitrification. The model accounts for soil NH_4^+ volatilization at the soil surface
161   when NH_4^+ in NH_4^+-containing fertilizers (e.g., urea) is converted to ammonia gas, depending upon pH
162   (*Huang and Gerber*, 2015). The soil NH_4^+ volatilization in the model is also affected by the anoxic condition,
163   which increases under a higher temperature and relatively lesser soil anoxic condition. The model accounts
164   for the impacts of pH on nitrification, denitrification, and volatilization rates (*Li et al.*, 2000; *Xu-Ri and*
165   *Prentice*, 2008). We prescribe the soil pH from the Global Soil Dataset for Earth System Modeling dataset
166   (GSDE) (*Shangguan et al.*, 2014).

167

168   **S1.2.5: LPX-Bern**

169   The implementation of nitrogen dynamics in LPX-Bern is based on the work of *Xu-Ri and Prentice* (2008).
170   Nitrogen uptake by plants is governed by their demand and the availability of nitrogen in two soil pools
171   representing ammonium and nitrate. Nitrogen from deposition and fertilization are added to these inorganic
172   soil pools. Losses include ammonium volatilization, nitrate leaching as well as N_2O and NO production
173   during nitrification and N_2O, NO and N_2 production during denitrification. Aerobic nitrification of
174   ammonium is dependent on soil temperature (T_{soil}) and indirectly on soil water content due to the
175   partitioning of wet and dry soil:

176

177    $R_{nit} = max_{nit} f_1(T_{soil}) C_{NH4,dry}$ (10)

178

179   where $max_{nit} = 0.92\ day^{-1}$ is the daily maximum nitrification rate at 20°C.

180 Anaerobic denitrification of nitrate in wet soil depends on labile carbon availability and soil temperature:

182 $$R_{den} = R_{mb}/(R_{mb} + K_{mb})f_2(T_{soil})C_{NO3,wet}/(C_{NO3,wet} + K_n) \qquad (11)$$

184 The parameters K_{mb} and K_n are taken from *Xu-Ri and Prentice* (2008) and R_{mb} is the microbiotical soil
185 respiration. The amount of nitrogen lost as N_2O due to nitrification and denitrification is modelled as a
186 function of soil temperature, water content and the respective process rate.

188 **S1.2.6: O-CN**

189 The treatment of inorganic soil nitrogen dynamics in O-CN follows largely *Xu-Ri and Prentice* (2008). O-
190 CN (*Zaehle and Friend*, 2010) considers N losses to NH_3 volatilisation, NOx, N_2O and N_2 production and
191 emission, as well as NH_4 and NO_3 leaching. Inorganic nitrogen dynamics in the soil are tightly coupled to
192 plant uptake and net mineralization. The anaerobic volume fraction of the soil is estimated by an empirical
193 function of the fractional soil moisture content (*Zaehle et al.*, 2011). The fraction of ammonium in the
194 aerobic part of the soil is subject to nitrification, according to:

196 $$R_{nit} = vmax_{nit}f(T1)f(pH1)C_{NH4} \qquad (12)$$

198 where *f(pH1)* is the soil pH response functions for nitrification (*Li et al.*, 1992; *Xu-Ri and Prentice*, 2008),
199 and *vmax_{nit}* is the maximum daily nitrification rate under 20°C and favourable pH conditions (*Xu-Ri and*
200 *Prentice*, 2008).

202 Gross denitrification of the fraction of nitrate under anoxic conditions is modelled as:

204 $$R_{den} = R_{mb}/(R_{mb} + K_{mb})f(T2)f(pH2)C_{NO3}/(C_{NO3} + K_n) \qquad (13)$$

206 where *f(pH2)* is the soil pH response functions for denitrification (*Li et al.*, 1992; *Xu-Ri and Prentice*, 2008),
207 R_{mb} is the soil microbial respiration rate, and K_{mb} and K_n parameters taken from *Li et al.* (1992).

209 The N_2O production from nitrification and denitrification is then calculated as:

211 $$R_{N2O} = a_{nit}f(T1)R_{nit} + b_{den}f(T2)f(pH3)R_{den} \qquad (14)$$

213 where a_{nit} and b_{denit} are fraction loss constants, *f(pH3)* is a pH-modifier changing the degree of denitrification
214 producing N_2O versus NO_x or N_2 (*Zaehle et al.*, 2011). Emissions of volatile compounds are simulated
215 using the empirical emission of *Xu-Ri and Prentice* (2008).

217 **S1.2.7: ORCHIDEE**

218 Modeling of the mineral N dynamics by the ORCHIDEE model originates from the formulations used in
219 the O-CN (*Zaehle and Friend*, 2010). It is composed of five pools for ammonium/ammoniac, nitrate, NOx,
220 nitrous oxide, and di-nitrogen forms. N_2O production in both nitrification and denitrification processes are
221 represented.

223 The potential daily rate of nitrification, R_{nit}, occurs only on the aerobic fraction of the soil and is a function
224 of temperature, pH, and ammonium concentration (C_{NH4}):

226 $$R_{nit} = (1 - f(WFPS))f(T1)f(pH1)k_{nit}C_{NH4} \qquad (15)$$

228 where k_{nit} is the reference potential NO_3^- production per mass unit of ammonium.

S1.2.8: VISIT

The nitrogen cycle scheme of VISIT is composed of three organic soil nitrogen pools (microbe, litter, and humus), two inorganic soil nitrogen pools (ammonium and nitrate), and vegetation pools. Fertilizer is considered as an input to the ammonium and nitrate pools at a fixed ratio, and manure as an input into the litter organic nitrogen pool. N_2O emissions through nitrification and denitrification are estimated using the scheme developed by *Parton et al.* (1996). Nitrification-associated N_2O emission ($R_{nit,N2O}$) is evaluated as follows,

$$R_{nit,N2O} = f(WFPS)f(pH1)f(T1)(K_{max} + F_{max}f(NH4)) \tag{16}$$

where K_{max} is the soil-specific turnover coefficient; F_{max} is the parameter of maximum nitrification gas flux; and $f(NH_4)$ is the effect of soil ammonium on nitrification. Denitrification-associated N_2O emission ($R_{den,N2O}$) is evaluated by the following equation:

$$R_{den,N2O} = R_{den}(1 + R_{N2/N2O}) \tag{17}$$

$$R_{den} = min(f(NO_3), f(CO_2)) \times f(WFPS) \tag{18}$$

where $R_{N2/N2O}$ is the fractionation coefficient, which is also a function of WFPS, soil nitrate, and heterotrophic respiration, $f(NO_3)$ is the maximum denitrification rate in high soil respiration rate condition, $f(CO_2)$ is the maximum denitrification rate in high NO_3^- levels, and $f(WFPS)$ is the effect of WFPS on denitrification rate.

N_2O production by nitrification ($R_{N2O,nit}$, g N-$N_2O/m^2/d$) is expressed as a function of the potential daily rate of nitrification (R_{nit}, g N-$NO_3^-/m^2/d$), temperature and the water content as shown in *Zhang et al.* (2002).

$$R_{N2O,nit} = f(WFPS)f(T1)R_{nit}p_{N2O,nit} \tag{19}$$

where $p_{N2O,nit}$ (g N-N_2O (g N-NO_3^-)$^{-1}$) is the reference N_2O production per mass unit of NO_3^- produced by nitrification. The denitrification occurs on the anaerobic fraction of the soil which is computed as a function of the water-filled porosity ($f(WFPS)$) and is controlled by temperature, pH, soil NO concentration and denitrifier microbial activity (a_{microb}, g m^{-2}) (*Li et al.*, 2000).

$$R_{N2O,den} = f(WFPS)f(T2)f(pH)f(NO)p_{N2O,den}a_{microb} \tag{20}$$

where $f(NO)$ is a Michaelis-Menten shape function and $p_{N2O,den}$ is the reference N_2O production per mass unit of denitrifier microbes.

S2 The FAOSTAT inventory

The FAOSTAT emissions data (*FAO*, 2022) are computed at Tier 1 following *IPCC* (2006), Vol. 4. The overall equation is as follows:
Direct emissions are estimated at the country level, using the formula:

$$Emission = A * EF \tag{21}$$

where emission represents kg N yr^{-1}; *A* represents the amount of N in the following items (annual synthetic N applications/manure applied to soils/manure left on pasture/manure treated in manure management systems/crop residue/biomass burned amount) in kg N yr^{-1}; *EF* = Tier 1, default IPCC emission factors, expressed in kg N/kg N.

279
280 Indirect emissions are estimated at the country level, using the formula:

282 $$Emission = A_{v\&l} * EF \tag{22}$$

284 where emission represents kg N yr^{-1}; $A_{v\&l}$ represents the fraction of manure/synthetic N fertilizers that
285 volatize as NH_3 and NO_x and are lost through runoff and leaching in kg N yr^{-1}; EF = Tier 1, default IPCC
286 emission factors, expressed in kg N/kg N.

288 Synthetic N fertilizers: N_2O from synthetic fertilizers is produced by microbial processes of nitrification
289 and denitrification taking place on the addition site (direct emissions), and after volatilization/redeposition
290 and leaching processes (indirect emissions).

292 Manure management: The term manure includes both urine and dung (i.e., both liquid and solid material)
293 produced by livestock. N_2O is produced directly by nitrification and denitrification processes in the manure,
294 and indirectly by nitrogen (N) volatilation and redeposition processes.
295 Manure applied to soils: N_2O is produced by microbial processes of nitrification and denitrification taking
296 place on the application site (direct emissions), and after volatilization/redeposition and leaching processes
297 (indirect emissions).

299 Manure left on pastures: N_2O is produced by microbial processes of nitrification and denitrification taking
300 place on the deposition site (direct emissions), and after volatilization/redeposition and leaching processes
301 (indirect emissions).

303 Crop Residue: N_2O emissions from crop residues consist of direct and indirect emissions from nitrogen (N)
304 in crop residues left on agricultural fields by farmers and from forages during pasture renewal (following
305 the definitions in the IPCC guidelines (*IPCC*, 2006)). Specifically, N_2O is produced by microbial processes
306 of nitrification and denitrification taking place on the deposition site (direct emissions), and leaching
307 processes (indirect emissions).

309 Cultivation of organic soils: The FAOSTAT domain "Cultivation of organic soils" contains estimates of
310 direct N_2O emissions associated with the drainage of organic soils – histosols – under cropland and grazed
311 grassland.

313 Burning-savanna: N_2O emissions from the burning of vegetation biomass in the land cover types: Savanna,
314 Woody Savanna, Open Shrublands, Closed Shrublands, and Grasslands. Burning-crop residues: N_2O
315 produced by the combustion of a percentage of crop residues burnt on-site. Burning-biomass: N_2O
316 emissions from the burning of vegetation biomass in the land cover types: Humid tropical forests, other
317 forests, and organic soils.

319 **S3 The EDGAR v7.0 inventory**

320 The new online version, EDGAR v7.0 (https://edgar.jrc.ec.europa.eu/dataset_ghg70) incorporates a full
321 differentiation of emission processes with technology-specific emission factors and additional end-of-pipe
322 abatement measures and as such updates and refines the emission estimates. The emissions are modelled
323 based on the latest scientific knowledge and available global statistics primarily from International Energy
324 Agency (*IEA*, 2021) for energy related sectors, FAO statistics (*FAO*, 2022) for agriculture, which were
325 complemented for the rest of sectors with United States Geological Survey (USGS), International Fertiliser
326 Association (IFA), Gas Flaring Reduction Partnership (GGFR)/U.S. National Oceanic and Atmospheric
327 Administration (NOAA) and World Steel Association (worldsteel) recent statistics; the methods are those
328 recommended by *IPCC* (2006). Official data submitted by the Annex I countries to the United Nations

329 Framework Convention on Climate Change (UNFCCC) and to the Kyoto Protocol are used to some extent,
330 particularly regarding control measures implemented since 1990 that are not described by international
331 statistics. A fast-Track approach was used to extend the N_2O emission time series for the latest years up to
332 2021 (*Crippa et al.*, 2021; *Crippa et al.*, 2022).
333
334 The N_2O emission factors for direct soil emissions of N_2O from the use of synthetic fertilizers, from manure
335 used as fertilizers, and from crop residues are taken from *IPCC* (2006), which updated the default IPCC
336 emission factor in the IPCC Good Practice Guidance (2000) with a 20% lower value. N_2O emissions from
337 the use of animal waste as fertilizer are estimated considering both the loss of N that occurs from manure
338 management systems before manure is applied to soils and the additional N introduced by bedding material
339 (*Janssens-Maenhout et al.*, 2019). N_2O emissions from fertilizer use and CO_2 from urea fertilization are
340 estimated based on IFA and FAO recent statistics.
341
342 N_2O emissions from manure management are based on the distribution of manure management systems
343 from Annex I countries reporting to the UNFCCC, *Zhou et al.* (2007) for China and *IPCC* (2006) for the
344 rest of the countries.
345
346 Different N_2O emission factors are applied to tropical and non-tropical regions. N and dry matter content
347 of agricultural residues are estimated from the cultivation area and yield for 24 crop types from *FAO* (2022)
348 and using emission factors of *IPCC* (2006).
349
350 Indirect N_2O emissions from leaching and runoff of nitrate are estimated from N input to agricultural soils.
351 Leaching and runoff are assumed to occur in all agricultural areas except non-irrigated dryland regions,
352 which are identified with maps of FAO Geonetwork (https://www.fao.org/land-water/databases-and-
353 software/geonetwork/en/). The fraction of N lost through leaching and runoff is based on the study of *Van*
354 *Drecht et al.* (2003). The updated emission factor for indirect N_2O emissions from N leaching and run-off
355 from the *IPCC* (2006) guidelines is selected, while noting that it is 70% lower than the mean value of the
356 1996 IPCC Guidelines and the IPCC Good Practice Guidance *IPCC* (1996; 2000).
357
358 Indirect N_2O emissions from atmospheric deposition of N of NO_x and NH_3 emissions from non-agricultural
359 sources, mainly fossil fuel combustion, are estimated using N in NO_x and NH_3 emissions from these sources
360 as activity data, based on EDGAR v7.0 database for these gases. The same emission factor from *IPCC*
361 (2006) is used for indirect N_2O from atmospheric deposition of N from NH_3 and NOx emissions, as for
362 agricultural emissions (*Janssens-Maenhout et al.*, 2019).
363
364 The uncertainties for EDGAR N_2O emissions estimated by *Solazzo et al.* (2021) are based primarily on the
365 uncertainties in emissions factors and activity data statistics from the *IPCC* (2006). Globally, these
366 emissions are accurate within an interval of ±113 for energy, -12% to +16% for industrial processes and
367 product use, -225 to +302 for agriculture, -159% to 203% for waste and ±112% for others; the most
368 uncertain emissions are those related to N_2O from waste and agriculture.
369
370 **S4 The UNFCCC inventory (need description of UNFCCC)**

371 The UNFCCC collects detailed data on GHG emissions from its parties. Following extensive guidance
372 developed by IPCC (*Buendia et al.*, 2019; *Eggleston et al.*, 2006), parties to the convention prepare national
373 GHG inventories, including emissions (and sinks) of N_2O. All anthropogenic activities are covered, in
374 agriculture both direct and indirect N_2O emissions are included. While IPCC basically provides emission
375 factor approaches, parties are encouraged to take account of national specificities, use national factors and
376 data, wherever available, or develop emission models, with adequate scientific proof provided.
377 Combustion-related emissions and emissions from industrial processes may take advantage of emission

378 monitoring or specific plant operation conditions, if provided. Emission processes that are not associated
379 with anthropogenic activities are also not covered in the inventories.
380
381 Obligations and quality of data provided differ strongly by country category. High scrutiny is put on GHG
382 inventories from countries listed in Annex-I of the convention (Annex-I countries include most European
383 countries, U.S. and Canada, Australia and New Zealand, and Japan). Annex-I countries are obliged to
384 provide annual national inventories in considerable detail and have to be very transparent also in terms of
385 methodology used and underlying information. Each year, time-series of emissions and underlying data
386 since 1990 (in a few cases, alternative base years are used) up to the pre-previous year are freshly provided
387 in April each year (e.g., in April 2023 data up to the year 2021 had to be provided), leading to a
388 homogeneous data series. Reports and emission data are provided (to UNFCCC, and to all users from the
389 UNFCCC web site at https://unfccc.int/reports) in standardized format such that they can be transferred to
390 databases. National results are routinely being checked and evaluated by expert teams in form of specific
391 internal and external audits to assure data quality and consistency.
392
393 National information is highly relevant also for non-Annex I countries to the UNFCCC and is being
394 collected and distributed by UNFCCC as well. Requirements are much less stringent, however, as parties
395 are expected to provide data only according to their own capabilities and the support they get from other
396 countries. The so-called Biannual Update Reports are to be prepared every other year only. While in
397 principle following the same IPCC guidance, commitments to format, timing, and quality assessment are
398 by far less stringent, and the own ambition level of the respective party (country) may determine much of
399 the outcome. In any case, self-reporting of a country always also means the party is willing to take the
400 responsibility of the emissions reported.
401
402 The "EDGAR/UNFCCC" dataset used in this paper utilizes the database for Annex-1 countries for
403 emissions from fossil-fuel consumption, industrial processes, waste and wastewater, and merges with the
404 respective set derived from EDGARv7.0 for all remaining countries.
405
406 **S5.1 The SRNM model: Flux upscaling model**

407 The SRNM model (Wang et al., 2020) was applied to simulate direct cropland-N_2O emissions. In SRNM,
408 N_2O emissions were simulated from N application rates using a quadratic relationship, with spatially
409 variable model parameters that depend on climate, soil properties, and management practices. The original
410 version of SRNM was calibrated using field observations only from China (Zhou et al., 2015). In this study,
411 we used the global N_2O observation dataset to train it to create maps of gridded annual emission factors of
412 N_2O and the associated emissions at 5-minute resolution from 1901 to 2014(Cui et al., 2021). The gridded
413 EF and associated direct cropland-N_2O emissions are simulated based on the following equation:
414
415

416 $$E_{ijt} = \alpha_{ij} N_{ijt}^2 + \beta_{ij} N_{ijt} + \varepsilon_{ijt}, \quad \forall i \tag{23}$$

417 where

418 $$\alpha_{ij} \sim N\left(\sum_k \left(x_k \lambda_{ijk} \right), \sigma_{ijk}^2 \right), \quad \beta_{ij} \sim N\left(\sum_k \left(x_k \phi_{ijk} \right), \sigma_{ijk}'^2 \right) \tag{24}$$

419 $$\lambda_{ijk} \sim N\left(\mu_{ijk}, \omega_{ijk}^2 \right), \quad \phi_{ijk} \sim N\left(\mu_{ijk}', \omega_{ijk}'^2 \right), \quad \varepsilon_{ijt} \sim N\left(0, \tau^2 \right) \tag{25}$$

420 and i denotes the sub-function of N_2O emission ($i=1, 2, …, I$) that applies for a sub-domain division W_i of
421 six climate or soil factors, j represents the type of crop ($j=1-2$, 1 for upland crops and 2 for paddy rice), k is
422 the index of climate or soil factors ($k=1-6$, i.e., soil pH, clay content, SOC, BD, the sum of cumulative
423 precipitation and irrigation, mean daily air temperature). W_i denotes a set of the range of multiple x_k. E_{ijt}

424 denotes direct N_2O emission flux (kg N ha^{-1} yr^{-1}) estimated for crop type j in year t in the ith sub-domain,
425 N_{ijt} is N application rate (kg N ha^{-1} yr^{-1}), and a_{ij} and b_{ij} are defined as summation of the product of x_k and l_{ijk}
426 over k. The random terms l and f are assumed to be independent and normally distributed, representing the
427 sensitivity of a and b to x_k. e is the model error. m and $m\cent$ are the mean effect of x_k for a and b, respectively.
428 s, $s\cent$, w, $w\cent$, and t are standard deviations. Optimal sub-domain division, associated parameters mean
429 values and standard deviations were determined by using the Bayesian Recursive Regression Tree version
430 2 (BRRT v2), constrained by the extended global cropland-N_2O observation dataset. The detailed
431 methodological approach of the BRRT v2 is described by Zhou et al (2015).
432
433 **S5.2 Global cropland N_2O observation dataset**

434 We aggregated cropland N_2O flux observation data from 180 globally distributed observation sites from
435 online databases, on-going observation networks, and peer-reviewed publications (Figure S1). Chamber-
436 based observations were only included in this dataset. These data repositories are as follows: the
437 NitroEurope, CarbonEurope, GHG-Europe (EU-FP7), GRACEnet, TRAGnet, NANORP, and 14 meta-
438 analysis datasets (*Decock*, 2014; *Harris et al.*, 2014; *Helgason et al.*, 2005; *Hénault et al.*, 2005; *Hickman*
439 *et al.*, 2014; *Kim et al.*, 2013a; *Kim et al.*, 2013b; *Lehuger et al.*, 2011; *Leppelt et al.*, 2014; *Rochette and*
440 *Janzen*, 2005; *Sacks et al.*, 2010; *Shcherbak et al.*, 2014; *Stehfest and Bouwman*, 2006; *Walter et al.*, 2015).
441 Four types of data were excluded from our analysis: (i) observations without a zero-N control for
442 background N_2O emission, (ii) observations from sites that used controlled-release fertilizers or nitrification
443 inhibitors, (iii) observations not covering the entire crop growing season, (iv) observations made in
444 laboratory or greenhouse. We then calculated cropland-N_2O emissions as the difference between observed
445 N_2O emission (E) and background N_2O emission (E_0). Values of EF were estimated for each nonzero N
446 application rate (N_a) as direct cropland-N_2O emission divided by N_a: $EF = (E - E_0)/N_a$. This yielded a
447 global dataset of direct cropland-N_2O emissions, N-rate-dependent N_2O EFs and fertilization records from
448 each site (i.e., 1,052 estimates for upland crops from 152 sites and 154 estimates for paddy rice from 28
449 sites), along with site-level information on climate, soils, crop type, and relevant experimental parameters.
450 Total numbers of sites and total measurements in the dataset were more than doubled those for previous
451 datasets of N_2O EF. The extended global N_2O observation network covered most of fertilized croplands,
452 representing a wide range of environmental conditions globally. For each site in our dataset, the variables
453 included four broad categories: N_2O emissions data, climate data (cumulative precipitation and mean daily
454 air temperature), soil attributes (soil pH, clay content, SOC, BD), and management-related or experimental
455 parameters (N application rate, crop type). More details on global cropland N_2O observation dataset can be
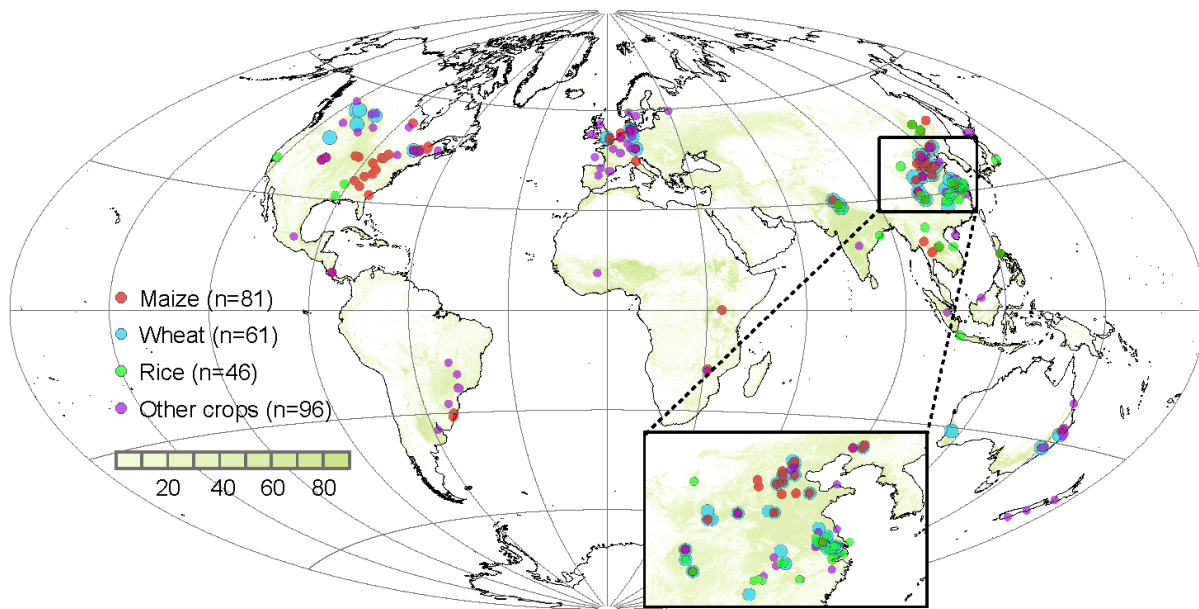456 found in *Cui et al.* (2021).
457

Figure S1 Global observation dataset of N$_2$O EF for direct soil emissions. Green area indicates the harvested areas of all crops derived from the Earthstat. Sites are indicated in different colors for maize, wheat, rice, and other crops.

S5.3 Gridded input datasets:

The updated SRNM model was driven by many input datasets, including climate, soil properties, agricultural management practices (e.g., fertilization, tillage, irrigation), as well as the historical distribution of cropland. Cumulative precipitation and mean daily air temperature over the growing season were acquired from the CRU TS V4.06 climate dataset (0.5-degree resolution) (*Harris et al.*, 2014), where growing season in each grid cell was identified following *Sacks et al.* (2010)The patterns of SOC, clay content, BD, and soil pH were acquired from the HWSD v1.2 ((*Berdanier and Conant*, 2012), 1-km resolution). Both climate and soil properties were re-gridded at 5-arc-minute spatial resolution using a first-order conservative interpolation widely used in the CMIP5 model intercomparison (*Yang et al.*, 2017). The annual cropland area at 5-arc-minute spatial resolution from 1961 to 2020 was obtained from the History Database of the Global Environment (HYDE 3.2.1) (*Goldewijk et al.*, 2017).

For fertilization, crop-specific N fertilizer inputs (including synthetic N fertilizers, crop residues and manure), fertilizer types, and placement during 1961-2020 were obtained from Adalibieke et al., (2023). The frequency (i.e., one or multiple times) of N fertilization were the same as *Cui et al.* (2021) and we assumed that the frequency remained constant during the study period. For tillage, the fraction of tillage by crop during 1961-2020 was obtained from Adalibieke et al., (2023), which was constructed with the country and province (or state) level no-tillage area data during 1961-2020 and downscaled to grid with the method of *Porwollik et al.* (2019). For irrigation, the History Database of the Global Environment (HYDE version 3.2) (*Goldewijk et al.*, 2017) and the MIRCA2000 dataset (*Portmann et al.*, 2010) were used to compile the global crop-specific irrigation proportion data from year 1961 to 2020. Categories of cropland in HYDE provided new distinctions with irrigated and rain-fed crops (upland crops, other than rice), irrigated and rain-fed rice during 1960-2017. The national-level dataset of "Agricultural area actually irrigated" was obtained from (*FAO*, 2022), which was used to scale the baseline year 2015 maps of irrigated area from HYDE over the period 2016-2020. The area of irrigated upland crops from HYDE was first disaggregated

12

488   into 21 crops based on the irrigated proportion from MIRCA2000 for per grid cell. We assumed an even
489   share of irrigated area by each upland crop during the period 1961-2020, like MIRCA2000. Finally, the
490   crop-specific irrigated area was masked by reporting harvested area, then the irrigated proportion of each
491   crop can be calculated as the crop-specific irrigated area divided by the physical area of each crop. For rice,
492   we further divided irrigated rice into continuously and intermittently flooded systems as provided by *Cui*
493   *et al.* (2021), and we assumed that the irrigation proportion was kept the same during the study period.
494
495   **S6 Global N flow in aquaculture**

496   We applied the IMAGE-GNM aquaculture nutrient budget model for shellfish and finfish (*Bouwman et al.*,
497   2013; *Bouwman et al.*, 2011) to calculate the nutrient flows in aquaculture production systems. These flows
498   comprise feed inputs, retention in the fish, and nutrient excretion. Individual species within crustaceans,
499   seaweed, fish and molluscs are aggregated to the International Standard Statistical Classification of Aquatic
500   Animals and Plants (ISSCAAP) groups (*FAO*, 2022), for which production characteristics are specified.
501   Feed and nutrient conversion rates are used for each ISSCAAP group to calculate the feed and nutrient
502   intake based on production data from FAO (*FAO*, 2020). Feed types include home-made aquafeeds and
503   commercial compound feeds with different feed conversion ratios that also vary in time due to efficiency
504   improvement; in addition, the model accounts for algae in ponds, that are often fertilized with commercial
505   fertilizers or animal manure, consumed by omnivore fish species like carp. A special case is the filter-
506   feeding bivalves that filter seston from the water column, and excrete pseudofeces, feces and dissolved
507   nutrients. Based on production data and tissue/shell nutrient contents, the model computes the nutrient
508   retention in the fish. Using apparent digestibility coefficients, the model calculates outflows in the form of
509   feces (i.e., particulate nutrients) and dissolved nutrients. Finally, nutrient deposition in pond systems and
510   recycling are calculated. For computing the N_2O emissions, we consider the amount of N released to the
511   environment, i.e., the difference between N intake and N in the harvested fish, which includes all the
512   nutrient excretion. Since in pond cultures part of that N is managed, we made the amount of N recycling
513   explicit, as well as ammonia emissions from ponds. This is to avoid double counting when computing N_2O
514   emissions from crop production.
515
516   **S7 Continental Shelves N_2O fluxes**

517   N_2O emissions from the global ocean do not include the contribution from continental shelves and are added
518   here using the extended mask of *Laruelle et al.* (2017) to delineate the coastal ocean. This mask excludes
519   estuaries and inland water bodies, while its outer limit is set 300 km away from the shoreline. Within this
520   coastal ocean domain, gridded N_2O emissions were calculated using one data-driven estimate and three
521   high-resolution model estimates from two distinct models, all interpolated on the same 0.25° x 0.25° grid.
522   Models and data are each covering different time-periods and only one climatology is provided, keeping
523   the original timespan of each product: 1988-2017 for the observation-based product that relied on a random-
524   forest (RF) algorithm to interpolate N_2O data (*Yang et al.*, 2020) from the MEMENTO database (MEM-
525   RF) (*Kock and Bange*, 2015), 1998-2018 for the estimate relying on the high-resolution configuration
526   (*Berthet et al.*, 2019) of the global ocean-biogeochemical component of CNRM-ESM2-1 (CNRM-0.25°),
527   1998-2013 and 2006-2013 for the estimates relying on the ECCO-Darwin model running at 1/3° (ECCO-
528   Darwin1) and 1/6° (ECCO-Darwin2), respectively. The resulting climatology can be considered as broadly
529   representative of the last 2-3 decades. Each product is further described as follows:
530
531   **S7.1 MEM-RF**

532   The N_2O air-sea flux reconstruction by *Yang et al.* (2020) is based on a synthesis of over 158,000
533   observations of N_2O mixing ratio, partial pressure, and concentration in the surface ocean from the
534   MEMENTO database (https://memento.geomar.de) (*Kock and Bange*, 2015) and additional cruises
535   (Dataset S1) (*Yang et al.*, 2020). N_2O measurements are converted to surface N_2O mixing ratio anomalies
536   using observations from the NOAA atmospheric flask dataset (*Hall et al.*, 2007), and extrapolated to a 0.25-

537   degree resolution global monthly climatology using an ensemble of 100 random forest realizations. The
538   random forest algorithm predicts N_2O mixing ratio anomalies based on their relationship to oceanographic
539   predictors that include hydrographic variables, nutrients, oxygen, chlorophyll, net primary production, and
540   seafloor depth. Reconstructed mixing ratio climatologies are used to estimate air-sea fluxes by applying a
541   commonly used gas exchange parameterization (*Wanninkhof*, 2014). Two formulations of piston velocity
542   are adopted: one based on a quadratic dependence on wind speed (*Wanninkhof*, 2014), and one that
543   explicitly accounts for bubble-mediated fluxes (*Liang et al.*, 2013). Sea ice cover, surface temperature,
544   salinity and atmospheric pressure are taken from ERA5 reanalysis (*Hersbach et al.*, 2017). Calculations are
545   performed with two high-resolution wind products (ERA5 and CCMP) that are available at 0.25, 6-hourly
546   resolution for the period from 1988 to 2017, yielding four permutations of the piston velocity. The resulting
547   ensemble of 400 global N_2O air–sea flux estimates is averaged in time to obtain monthly mean climatologies.
548   A description of the dataset and methods is presented in *Yang et al.* (2020). The code used to produce these
549   datasets is archived on a public GitHub repository at https://github.com/yangsi7/mapping-ocean-n2o (DOI:
550   10.5281/zenodo.3757194).
551
552   **S7.2 CNRM-0.25°**

553   N_2O fluxes have been inferred from the global ocean-biogeochemical component of CNRM-ESM2-1
554   (*Séférian et al.*, 2019) run at 0.25° horizontal resolution with 75 vertical levels in the ocean. This high-
555   resolution configuration is described in *Berthet et al.* (2019) and is based on the NEMOv3.6 oceanic model
556   (*Madec*, 2008), the multi-category sea ice model GELATOv6 (*Salas y Mélia*, 2002) and the PISCESv2-gas
557   model for marine biogeochemistry (*Aumont et al.*, 2015), which includes an updated version of (*Martinez-*
558   *Rey et al.*, 2015) for the marine N_2O module. The simulation was first spun-up during 300 years under
559   preindustrial conditions and then has been forced by the OMIP2-compliant JRA55-do-1-5 atmospheric
560   reanalysis (*Tsujino et al.*, 2020; *Tsujino et al.*, 2018) considering the historical evolution of CO_2 and N_2O
561   in the atmosphere since the year 1850. Boundary conditions for nitrogen deposition and riverine inputs are
562   prescribed from monthly climatologies. The suboxic production of N_2O uses the oxygen-dependent
563   formulation of *Jin and Gruber* (2003) and is enhanced at low oxygen concentrations. This formulation
564   encompasses N_2O production during remineralization, nitrification and grazing, as well as a sink term
565   corresponding to N_2O consumption under anoxic conditions by denitrification. The oceanic N_2O partial
566   pressure is computed based on the surface N_2O concentration and the N_2O solubility in the ocean. Sea-to-
567   air N_2O fluxes are then computed using the standard gas exchange parameterization of *Wanninkhof* (1992;
568   2014).
569
570   **S7.3 ECCO-Darwin & ECCO2-Darwin**

571   For this study we generated global air-sea fluxes of nitrous oxide (N_2O) from the global ocean by using two
572   models that include the same biogeochemical component but embedded in two different ocean physical
573   settings, ECCO2-Darwin and ECCO-Darwin.
574
575   The first model, ECCO2-Darwin model, is a global physical-biogeochemical ocean model with nominal
576   horizontal grid of 1/6 of degree therefore eddy-permitting at lower latitudes.
577   The second model is ECCO-Darwin, a global physical-biogeochemical ocean model with nominal
578   horizontal grid resolution of 1/3 of degree (Carroll et al., 2020). The ECCO-Darwin model is forced with
579   an atmospheric forcing corresponding to the 1992-present optimized with adjoint technique in order to
580   realistically represent the observed physical ocean climate variability. An extensive description of this
581   model run of ECCO2-Darwin including the optimized atmospheric forcing spanning from 2004 to 2013
582   can be found in Manizza et al., (2019, 2023) while for ECCO-Darwin a more detailed model description
583   can be found in Carroll et al., (2020). Both models have 50 vertical levels and in the top 100 m the model
584   is vertically resolved with 10-meter grid boxes.
585

586 The Darwin biogeochemical/ecological model used for this study explicitly represents the cycle of carbon,
587 oxygen, phosphorus, silica, and iron in the global ocean. It also has an ecosystem component representing
588 five groups of phytoplankton and two groups of zooplankton (Manizza et al., 2019, Carroll et al., 2020).
589
590 For this version of the model, we implemented a parameterization of the oceanic cycle of N_2O using the
591 scheme of Nevison et al., (2003) based on the oceanic oxygen cycle previously represented in ECCO2-
592 Darwin model (Ganesan et al., 2020). The air-sea gas flux of N_2O was parameterized according to
593 Wanninkhof (1992).
594
595 In the ECCO2-Darwin simulation the 2004-2005 period was discarded, and we used the 2006-2013 period
596 only for our analysis. However, the ECCO-Darwin numerical simulation was run for the 1992-2014 period,
597 but we discarded the inclusion of the output relative to the 1992-1996 period in our analysis due to the
598 model adjustment in this initial part of our numerical simulation. The results of these simulations were also
599 used in the study of Resplandy et al. (2023).
600
601 **S8 Open Ocean N_2O fluxes**
602 N_2O is produced in the open ocean by microbial activity during organic matter cycling in the subsurface
603 ocean, and its production pathways are influenced by the local environmental oxygen level. In the oxic
604 ocean N_2O is produced as a byproduct during the oxidation of ammonia to nitrate, mediated by ammonia
605 oxidizing bacteria and archaea. N_2O is also produced and consumed in sub- oxic and anoxic waters through
606 the action of marine denitrifiers during the multi-step reduction of nitrate to gaseous N. The oceanic N_2O
607 distribution therefore displays significant heterogeneity with background levels of 10-20 nmol/l in the well-
608 oxygenated ocean basins, high concentrations (> 40 nmol/l) in hypoxic waters, and N_2O depletion in the
609 core of ocean oxygen minimum zones (OMZs).
610
611 For this synthesis open ocean N_2O emissions to the atmosphere were compiled from four global ocean
612 biogeochemistry models/Earth System models that simulate the production, consumption and circulation
613 of oceanic N_2O (Table 6). N_2O flux exchange between ocean and atmosphere is derived using gas-exchange
614 parameterizations applied to modeled surface ocean N_2O. Versions of the four submitting models also
615 participated in the previous N_2O budget synthesis (*Tian et al.*, 2020a). Model details and updates to the
616 previous N_2O budget synthesis are summarized below.
617 The models differ in aspects of physical configuration (e.g., spatial resolution), meteorological forcing
618 applied at the ocean surface, and in their parameterizations of ocean biogeochemistry; specific details on
619 individual models are provided in the publications listed in Table 1. Towards this N_2O budget synthesis,
620 modelling groups reported grid-resolved ($1° \times 1°$ horizontal resolution) monthly estimates of ocean-
621 atmosphere N_2O fluxes for the period 1980-2020 (or for as many years as possible in that period).
622
623 **S8.1 U. Bern: Bern-3D**
624 N_2O fluxes are derived from the Bern-3D Earth System Model of Intermediate Complexity which includes
625 a prognostic marine biogeochemistry model (based on (*Parekh et al.*, 2008) and (*Tschumi et al.*, 2011)).
626 Configuration of the model for simulation of N_2O is outlined in *Battaglia and Joos* (2018). Model
627 simulations were run at a native resolution of horizontal resolution of 41 by 40 grid cells and 32
628 logarithmically scaled vertical layers. Modifications of the biogeochemistry model relevant for the N_2O
629 cycle include the assignment of organic matter remineralization to aerobic and anaerobic pathways
630 dependent on mean grid-cell dissolved oxygen level. N_2O is produced by nitrification as a product of
631 remineralization rate and a specified N_2O yield which has a functional form dependent on oxygen level (see
632 details in (*Battaglia and Joos*, 2018)). N_2O consumption by denitrification processes is represented by a
633 first-order kinetics formulation which also includes a dependence on local oxygen level to account for the
634 relative importance of denitrification-related N_2O production and consumption processes in each gridcell.
635 Measurements of dissolved N_2O (surface and interior) from the MEMENTO database (*Kock and Bange*,

636   2015) together with an ensemble of model runs are used to constrain the model parameters governing N_2O
637   production and consumption mechanisms. From a pre-industrial equilibrium state the model is forced by
638   historical CO_2 emissions, non-CO_2 radiative forcing, and land-use changes. N_2O in the atmosphere is
639   prescribed based on historical data.
640
641   **S8.2 CNRM: CNRM-ESM2-1**

642   N_2O fluxes are provided by the CNRM-ESM2-1 Earth System model. The ocean model component is based
643   on NEMO Version 3.6 (*Madec et al.*, 2017) and coupled to the GELATO sea ice model (*Salas y Mélia*,
644   2002) Version 6 and the marine biogeochemical model PISCESv2-gas (*Aumont et al.*, 2015). The spatial
645   model resolution follows the eORCA1L75 grid, with a nominal horizontal resolution of 1° and with higher
646   resolution in the tropics (increasing to ~(1/3)°). The model has 75 vertical levels with higher resolution
647   towards the ocean surface. The simulations were forced at the surface by the atmospheric state of JRA55-
648   do v1.5.0 (*Tsujino et al.*, 2018). Atmospheric N_2O concentration is given as annual means as specified by
649   CMIP6 protocols and is linearly interpolated in time. Parameterization of the marine N_2O cycle follows that
650   of *Martinez-Rey et al.* (2015) with some modifications. N_2O production is driven by an oxygen-dependent
651   yield of N_2O, which encompasses production from denitrification and nitrification processes. This
652   formulation also assumes a constant background yield representing N_2O production by nitrification and a
653   consumption of N_2O in suboxic conditions. Originally implemented by *Martinez-Rey et al.* (2015), the
654   marine N_2O parameterization has benefited from a recoding and an improved calibration presented in
655   *Berthet et al.* (2023). Further details of the model biogeochemistry and configuration are provided by
656   *Séférian et al.* (2019) and *Berthet et al.* (2019).
657
658   **S8.3 UVic2.9**

659   N_2O model fluxes are derived from the UVic2.9, Earth System Model of Intermediate Complexity with
660   prescribed monthly climatological winds (*Kalnay et al.*, 1996) and ice sheets (*Peltier*, 2004), configuration
661   outlined in *Landolfi et al.* (2017). Oceanic subsurface N_2O production is parameterized following (*Zamora*
662   *and Oschlies*, 2014), as a function of O_2 consumption with a linear O_2 dependency, inherently including
663   both nitrification and denitrification. In O_2-deficient waters (<4 mmol m^{-3}), denitrification becomes a sink
664   of N_2O consumed at a constant rate. The gradient driving the air-sea N_2O gas exchange, is computed online
665   based on departure of the surface ocean concentration from the saturation value using the solubility
666   coefficients of *Weiss and Price* (1980) and time-varying prescribed atmospheric N_2O concentrations
667   (historical and RCP8.5). The model was spun-up for 6000 years with preindustrial boundary conditions
668   (solar and volcanic and aerosol forcing, fixed atmospheric CO_2 of 280 ppm and N_2O of 276 ppb, and
669   preindustrial atmospheric N deposition).
670

671   **S8.4 UEA: NEMO-PlankTOM10.2**

672   N_2O model fluxes are derived from the NEMO-PlankTOM10.2 ocean model. The physical circulation
673   component is NEMO v3.1 (*Madec*, 2008), with horizontal resolution of 2° longitude, and a variable
674   latitudinal resolution (average ~1°) with higher resolution in the tropics and polar regions. The model has
675   30 vertical layers, with variable resolution ranging from 10m in the upper 100m to 500m at depths of 5000
676   m. The biogeochemical component relies on the marine ecosystem model PlankTOM10, which includes
677   representation of 10 plankton functional types (*Le Quéré et al.*, 2016). It has been extended by *Buitenhuis*
678   *et al.* (2018) to include nitrogen cycle processes, and prognostic and diagnostic models of N_2O production.
679   N_2O is produced from nitrification and denitrification pathways, with oxygen dependent yields employed
680   to account for varying production and consumption processes in hypoxic waters. Nitrogen cycle parameters
681   are optimized using ocean databases of dissolved N_2O (MEMENTO, *Kock and Bange* (2015)) nitrification
682   rates (*Yool et al.*, 2007), and surface ammonium concentrations (*Johnson et al.*, 2015; *Paulot et al.*, 2015).
683   Further details on model configuration are provided in (*Buitenhuis et al.*, 2018).
684

S9 Net N₂O emission from land cover change

This section mainly involves the calculation of post-deforestation N_2O emissions, deforestation induced N_2O reduction and N_2O emissions from forest regrowth (afforestation or reforestation). The methods include both bookkeeping and process-based modeling.

S9.1 Deforestation area, crop/pasture expansion and secondary forests

The LUH2 v2h (land use harmonization, http://luh.umd.edu) land use data was used to derive the deforestation area and its partition between crops and pastures during 1860−2020. LUH2 categorizes forest lands into forested primary land and potentially forested secondary land, while croplands are divided into C3 annual crops, C3 perennial crops, C4 annual crops, C4 perennial crops, and C3 N-fixing crops.

In the empirical computation of deforestation induced N_2O emissions, all sub-classes within each land use type were treated the same. Thus, only the annual transition area from forests to croplands or managed pasture was needed. In the process-based estimates, the DLEM model was improved to further account for the classifications of primary forests, secondary forests (further partitioned into established and newly converted by an age threshold of 15 years), croplands/pastures /rangelands (further partitioned into established and newly converted by an age threshold of seven nine years). Each land use type can be divided into several different plant functional types (PFTs). Specifically, within a grid cell, cropland can only be dominated by only one crop type. The pastures and rangelands can be either C3 type or C4 type. To generate the historical spatial distribution of PFTs, a potential vegetation map and the accompanied composition ratio map of each natural PFT acquired from the Synergetic Land Cover Product (SYNMAP) were jointly used with LUH2 v2h.

S9.2 Methods

The bookkeeping method was mainly applied to the tropical areas, where forests generally have high N_2O emissions. Specifically, the average tropical forest N_2O emission rate of 1.974 kg N_2O-N ha-1 yr-1 was adopted as the baseline. Two logarithmic response curves of soil N_2O emissions (normalized to the baseline) after deforestation were developed: $y = -0.31\ln(x) + 1.53$ and $y = -0.454\ln(x) + 2.21$. This form of the response functions can effectively reproduce the short-lived increase in soil N_2O emissions after initial forest clearing and the gradually declining emission rates of converted crops/pastures (*Melillo et al.*, 2001; *Verchot et al.*, 1999). Using these two curves and the baseline, we kept track of the N_2O reduction of tropical forests and the post-deforestation crop/pasture N_2O emissions at an annual timescale.

There are not many studies on N_2O emissions from secondary tropical forests that regrowth after crop or pasture abandonment. *Sullivan et al.* (2019) lumped together all forms of N "gas loss" including NO and N_2O for secondary forests across the tropics and the results showed gas loss gradually increases with age since the regrowth of secondary forest. *Keller and Reiners* (1994) also reported a gradual recovery of soil nitrate and soil emissions of N_2O and nitric oxide (NO) during 20 years of secondary forest succession, which however did not return to the level of the primary forests. In this study, using field observations from *Davidson et al.* (2007) and *Keller and Reiners* (1994), we regressed normalized N_2O emissions (relative to a reference mature forest) of secondary tropical forests with their ages as $y=0.0084x + 0.2401$ ($R^2 = 0.44$; unit of x is year). The derived y values were multiplied by tropical forest N_2O emissions estimated by NMIP2 models that do not distinguish secondary forests from primary forests.

The DLEM model was run with varying climate and CO_2 with other factors held constant to estimate forest baseline emissions and unfertilized crop/pasture emissions from 1860-2020. The climate data were acquired from CRUJRA, which is a fusion of the CRU and JRA reanalysis products at a spatial resolution of 0.5° × 0.5° and a daily time-step. The atmospheric CO_2 data were obtained from NOAA GLOBLVIEW-CO2 dataset (https://www.esrl.noaa.gov), which are derived from atmospheric and ice core measurements. In

17

734 the tropical area, both estimates from the DLEM model and the bookkeeping method were adopted, whereas
735 in extra-tropical area, we only adopted the DLEM outputs.
736
737 **S10 Inland water, estuaries, and coastal vegetation**
738
739 **S10.1 Dynamic Land Ecosystem Model-Terrestrial/Aquatic Continuum (DLEM-TAC)**
740 To quantify N_2O emissions from global inland waters (rivers, lakes, and reservoirs), we use a process-based
741 coupled terrestrial-aquatic model, which builds up on the Dynamic Land Ecosystem Model (DLEM).
742 DLEM-TAC is a fully distributed, process-based land surface model which couples the major land
743 processes (terrestrial hydrology, plant phenology and physiology, soil biogeochemistry) and aquatic
744 dynamics (lateral transport and in-stream biogeochemistry) (*Pan et al.*, 2021; *Tian et al.*, 2015; *Tian et al.*,
745 2020b; *Yao et al.*, 2020). The land component of DLEM-TAC explicitly simulates the carbon, nitrogen,
746 and water fluxes between plants, soil, and atmosphere, and the surface and drainage runoff and nitrogen
747 load from the land module are used as   input for   the aquatic module. The simulated nitrogen load
748 includes dissolved inorganic nitrogen (DIN), dissolved organic nitrogen (DON), particulate organic
749 nitrogen (PON), and runoffs, sewers as the initial condition of the aquatic module.
750
751 DLEM-TAC aquatic module calculated lateral water transport and the associated aquatic biogeochemical
752 processes by adopting a scale-adaptive scheme. The water transport scheme, which coupled hillslope flow,
753 subnetwork flow, and main channel flow, simulated the water transport processes within grid cells. In the
754 aquatic module, lakes and reservoirs were linked with small streams and large rivers, forming a river-lake-
755 reservoir corridor (*Wollheim et al.*, 2008)). Particularly, lakes that are linked to small streams are typically
756 small in size and are defined as small lakes, while those linked to large rivers are usually had large size and
757 are defined as large lakes; similarly, reservoirs that are linked to main channels are considered as large
758 reservoirs, while those that are linked to small streams are considered as small reservoirs. The incoming
759 flow of a linked river-lake-reservoir corridor drains to lakes first, and the outflow rate of lakes and reservoirs
760 is determined based on the predefined residence time obtained from the global lake dataset (*Lehner et al.*,
761 2011; *Messager et al.*, 2016; *Yao et al.*, 2022). The aquatic N module was developed based on the scale
762 adaptive water transport scheme, including lateral transport, decomposition of organic matter, particle
763 organic matter deposition, nitrification, and denitrification. The detailed description could be found in the
764 previous studies (*Pan et al.*, 2021; *Tian et al.*, 2020b; *Yao et al.*, 2020).
765
766 Following our previous work referring to the development of water transport and biogeochemistry, we
767 developed an inland water N_2O module within the aquatic biogeochemical component of the DLEM
768 framework (*Yao et al.*, 2020). The net fluxes of dissolved N_2O (including physical and biogeochemical
769 processes) in the main channel (high-order streams) and subnetwork (small rivers) are estimated as:
770

$$(\Delta M\_N2O) / \Delta t = Fa + Ywater + D - R - E \tag{26}$$

771 where M_N2O is the total mass of dissolved N_2O in the main channel or subnetworks (g N), Δt is the time
772 step, Fa is advective N_2O fluxes (g N d^{-1}), Ywater is the N_2O production within the water column (g N d^{-1}),
773 D is the dissolved N_2O from rainfall to rivers (i.e. deposition) (g N d^{-1}) with an initial concentration equal
774 to the atmospheric equilibrium N_2O concentration, R is the flux from N_2O reduction (g N d^{-1}) to nitrogen
775 gas, and E is the riverine N_2O efflux (g N d^{-1}) through the air-water interface.
776
777 Input data. The driving data of DLEM-TAC include the climate variables, atmospheric CO2 concentration,
778 land use change, nitrogen (N) deposition, N fertilizer, and manure application with a spatial resolution of
779 0.5°× 0.5°. The daily climate variables (precipitation, mean temperature, maximum temperature, minimum
780 temperature, and shortwave radiation) were obtained from the CRUNCEP dataset (https://vesg.ipsl.upmc.fr)

781 for 1901-2019. Climate data of each year during 1850-1900 was randomly sampled from 1901-1920.
782 Annual atmospheric CO2 concentration from 1900-2019 was obtained from the NOAA GLOBALVIEW-
783 CO2 dataset (https://www.esrl.noaa.gov). The annual land use change data was derived from a potential
784 natural vegetation map (synergetic land cover product) and a prescribed cropland area dataset from the
785 history database of the global environment v.3.2 (HYDE 3.2, ftp://ftp.pbl.nl/hyde). The data of N fertilizer,
786 manure N application, and N deposition data was obtained from (*Tian et al.*, 2022).

788 In the aquatic module, the required channel dataset included channel slope, channel width, and channel
789 length generated from the Hydroshed dataset (*Lehner et al.*, 2008) and DDM30 dataset (*Döll and Lehner*,
790 2002). The flow direction and distance data were obtained from the Dominant River Tracing (DRT) dataset.
791 For modeling water dynamics in lakes and reservoirs, we generated 0.5 grid level surface water area,
792 upstream area, volume, depth, and average residence time for lakes based on the Hydrolakes dataset
793 (*Messager et al.*, 2016), while the GRanD database provided the same information for reservoirs (*Lehner*
794 *et al.*, 2011).

796 Simulation protocol. DLEM-TAC simulations include three steps: equilibrium run, spin-up run and two
797 transit runs, one with dam operation close, and another one with dam operation open. First, the equilibrium
798 run is required to obtain the initial and steady condition of carbon, nitrogen, and water pool at the pre-
799 industrial level in each grid cell (*Thornton and Rosenbloom*, 2005). In this step, we held all the driving
800 forces such as climate data, atmospheric CO_2 concentration, land use data, and nitrogen additions consistent
801 with the first year's data we used in the simulation. Second, we conducted a 30-year spin-up run by
802 randomly selecting climate data within the 1850s (*Tian et al.*, 2012a). This step can alleviate the disturbance
803 of driving data changes in the transit run. Then we conduct the natural flow simulation with the dam model
804 temporarily closed, and all the driving forces change over time. After the natural flow simulation, we set
805 up a management flow simulation with the dam module open, specifically the dam module needs natural
806 flow in the previous run as model input.

808 **S10.2 Mechanistic Stochastic Modeling of N$_2$O emissions from large rivers, lakes, reservoirs, and**
809 **estuaries:**

811 To calculate the cascading loads of TN and TP delivered to each water body along the river–reservoir–
812 estuary continuum, we spatially routed all reservoirs from the GRanD database (*Lehner et al.*, 2011), with
813 river networks from Hydrosheds 15s (*Lehner et al.*, 2008) and, at latitudes above 50°N, Hydro1K
814 (http://edc.usgs.gov/products/elevation/gtopo30/hydro/), which were in turn connected to estuaries as
815 represented in the "Worldwide Typology of Nearshore Coastal Systems" of *Dürr et al.* (2011). In addition,
816 the global database HydroLAKES (*Messager et al.*, 2016) was used to topologically connect 1.4 million
817 lakes with a minimum surface area of 0.1 km^2 within the river network. Note that besides natural lakes,
818 HydroLAKES includes updated information on 6,796 reservoirs from the GRanD database, which was used
819 in the study of *Maavara et al.* (2019). In order to estimate the TN and TP loads to each water body, we then
820 relied on a spatially explicit representation of TN and TP mobilization from the watershed into the river
821 network (see (*Maavara et al.*, 2019) for details (*Bouwman et al.*, 2009; *Van Drecht et al.*, 2009).

823 For the estimation of N$_2$O emission, we applied two distinct model configurations, respectively named DS1
824 and DS2 in *Maavara et al.* (2019). DS1 estimates N$_2$O emissions from denitrification and nitrification based
825 on an EF of 0.9%, which is in the mean of published values (*Beaulieu et al.*, 2011), and the assumption that
826 N$_2$O production equals N$_2$O emissions (*Maavara et al.*, 2019). For DS2, the reduction of N$_2$O to N$_2$ during
827 denitrification if N$_2$O is not evading sufficiently rapidly from the water body is considered. The fluxes in
828 the model represent lumped sediment-water column rates and were resolved at the annual timescale. The
829 use of water residence time as an independent variable in both the mechanistic model and the upscaling
830 process introduces an important kinetic refinement to existing global N$_2$O emission estimates. Rather than

19

831 applying an average EF (directly scaling N_2O emissions to N inputs) to all water bodies, the use of water
832 residence time explicitly adjusts for the extent of N_2O production and emission that is kinetically possible
833 within the timeframe available in a given water body. Simulated N_2O emission rates were evaluated against
834 UNFCCC measurement-based upscaling methods applied to reservoirs (*Deemer et al.*, 2016) and rivers
835 (*Hu et al.*, 2016) as well as a UNFCCC observation-driven regional estimate of lake N_2O emissions based
836 on literature data (*Lauerwald et al.*, 2019).
837
838 **S10.3 Meta analysis-based N_2O emissions from large rivers**

839 Data from 70 published studies between 1998 and 2016 that provided N_2O emission from streams and rivers
840 were compiled by *Hu et al.* (2016). The N_2O emission factors (EF = N_2O /DIN) and emission rates (ER =
841 EF * DIN load, kg N_2O-N yr^{-1}) were calculated for each studied river. Exploratory multiple regression
842 analyses were conducted to predict EF and ER using various combinations of factors (N concentrations,
843 loads, yields, DOC: DIN, discharge, and watershed area) and different functions. Among them, DIN yield
844 (kg N yr^{-1} km^{-2}) was identified as the best predictor of EF and ER. Using the optimal model and DIN loads
845 for 6400 global rivers calculated by the NEWS2-DIN-S model (*McCrackin et al.*, 2014), we estimated
846 global riverine N_2O emissions (*Hu et al.*, 2016).
847
848 **S10.4 Stream and river N_2O emissions combining machine-learning and model-based upscaling**

849 *Marzadri et al.* (2021) developed a novel approach that combines a data-driven Random Forest Machine
850 Learning (RM-ML) model with a physically-based upscaling model to predict near global (neglecting
851 Arctic and Antarctic areas) riverine N_2O emissions flux (F*N_2O given by the ratio between the flux of N_2O,
852 FN_2O, and the in-stream flux of dissolved inorganic nitrogen species FDIN) from both surface (i.e. water
853 column) and subsurface (i.e. benthic zone and hyporheic zone) riverine environments. In particular, to
854 capture the local scale processes responsible for N_2O emissions and to provide estimations at different
855 spatial scales (from local reach up to the global scale) the model compute two different denitrification
856 Damköhler numbers (given by the ratio between a characteristics time of transport and a characteristics
857 time of denitrification (*Marzadri et al.*, 2021; *Marzadri et al.*, 2017)) starting from the hydro-morphological
858 and biogeochemical information provided by the RM-ML model. Model results at the local reach scale
859 shows that nearly 50% of the riverine N_2O emissions comes from small streams (i.e. widths lower than 10
860 m, although they represent only the 13% of the total riverine surface area worldwide) while at the large
861 scale predict a near-global annual riverine N_2O emissions around 72.8 GgN_2O-N/yr.
862
863 **S10.5 Meta-analysis based N_2O emissions from estuaries and coastal vegetation**

864 N_2O emissions from estuaries and coastal vegetated ecosystems were obtained from a meta-analysis of
865 observed N_2O fluxes (*Rosentreter et al.*, 2023). In brief, the meta-data analysis relies on a categorization of
866 estuaries into 'tidal systems and deltas', 'lagoons', and 'fjords'. Water-air N_2O fluxes from 123 estuary
867 sites globally were then compiled from peer-reviewed publications until the end of 2020. Coastal vegetation
868 comprises 'mangrove', 'salt marsh', and 'seagrass' ecosystems and N_2O sediment-water-air fluxes were
869 compiled from 55 sites globally from peer-reviewed publications until the end of 2020. A non-parametric
870 bootstrapping method (1000 iterations of the median of samples) was used to resample N_2O fluxes per unit
871 area for each estuary and coastal vegetation type in each of the 18 regions using the 'boot' function in the
872 package 'boot' in R software. Results from the bootstrapping output (minimum, Q1, median, mean, Q3,
873 maximum) were then scaled to the surface area of each estuary and coastal vegetation type in each of the
874 18 regions. If an ecosystem type had less than three sites in a region, we applied the global statistics of this
875 type in this region. Note that the meta-data analysis only provides flux assessments at the scale of the 18
876 regions.
877
878 **S11 Atmospheric inversion models**

879 Emissions were estimated using four independent atmospheric inversion frameworks (see Table 1). The
880 frameworks all used a Bayesian inversion method. The approach used here finds the maximum posteriori
881 (MAP), or optimal, estimate of emissions, that is, those, which when coupled to a model of atmospheric
882 transport, provide the best agreement to observed N_2O mixing ratios while being guided by their prior
883 probability. In this particular case, where both the likelihood and prior probability are assumed to be
884 distributed normally, the optimal emissions are equivalent to those that minimize the cost function,
885

$$J(\mathbf{x}) = \frac{1}{2}(\mathbf{x} - \mathbf{x_b})^T \mathbf{B}^{-1}(\mathbf{x} - \mathbf{x_b}) + \frac{1}{2}(\mathbf{y} - H(\mathbf{x}))^T \mathbf{R}^{-1}(\mathbf{y} - H(\mathbf{x}))$$

886 (27)
887

888 where $\mathbf{x}$ and $\mathbf{x_b}$ are, respectively, vectors of the multivariate means of the posterior and prior emission
889 distributions, $\mathbf{B}$ is the prior error covariance matrix for emissions, $\mathbf{y}$ is a vector of observed N_2O mixing
890 ratios, $\mathbf{R}$ is the observation error covariance matrix, and $H(\mathbf{x})$ is the model of atmospheric transport (for
891 details on the inversion method see (*Tarantola*, 2005)). The optimal emissions, $\mathbf{x}$, were found by solving
892 the first order derivative of equation (21):
893

$$J'(\mathbf{x}) = \mathbf{B}^{-1}(\mathbf{x} - \mathbf{x_b}) + (H'(\mathbf{x}))^T \mathbf{R}^{-1}(\mathbf{y} - H(\mathbf{x})) = 0$$

894 (28)
895

896 where $(H'(\mathbf{x}))^T$ is the sensitivity of the atmospheric observations to emissions, derived from an adjoint
897 model of transport. In frameworks INVICAT, PyVAR-CAMS and GEOS-Chem, equation (5b) was solved
898 using a variational approach (*Thompson et al.*, 2014; *Wells et al.*, 2015; *Wilson et al.*, 2014), which uses a
899 descent algorithm and computations involving the forward and adjoint models. In framework MIROC4-
900 ACTM (*Patra et al.*, 2018), equation (22) was solved directly by computing a transport operator, $\mathbf{H}$ from
901 integrations of the forward model, such that $\mathbf{Hx}$ is equivalent to $H(\mathbf{x})$, and taking the transpose of $\mathbf{H}$ (*Patra*
902 *et al.*, 2022).
903

904 Each of the inversion frameworks used a different model of atmospheric transport with different horizontal
905 and vertical resolutions (see Table 1). The transport models TOMCAT and LMDz5, used in INVICAT and
906 PyVAR-CAMS respectively, were driven by ECMWF ERA-5 and ERA-Interim wind fields respectively,
907 MIROC4-ACTM was driven by JRA-55 wind fields, and GEOS-Chem was driven by MERRA-2 wind
908 fields. While INVICAT, PyVAR-CAMS, and GEOS-Chem optimized the emissions at the spatial
909 resolution of the transport model, MIROC4-ACTM optimized the error in the emissions aggregated into 84
910 land and ocean regions. All frameworks optimized the emissions with monthly temporal resolution. The
911 transport models included an online calculation of the loss of N_2O in the stratosphere due to photolysis and
912 oxidation by $O(^1D)$ resulting in mean atmospheric lifetimes of between 118 and 129 years, broadly
913 consistent with recent independent estimates of the lifetime of 116±9 yr (*Prather et al.*, 2015)).
914

915 All inversions used N_2O measurements of discrete air samples from the National Oceanic and Atmospheric
916 Administration Carbon Cycle Cooperative Global Air Sampling Network (NOAA). In addition, discrete
917 measurements from the Commonwealth Scientific and Industrial Research Organisation network (CSIRO)
918 as well as in-situ measurements from the Advanced Global Atmospheric Gases Experiment network
919 (AGAGE), the NOAA CATS network, and from individual sites operated by University of Edinburgh (UE),
920 National Institute for Environmental Studies (NIES), the Finnish Meteorological Institute (FMI) and the
921 Japan Meteorological Agency (JMA) were included in INVICAT, PyVAR-CAMS and GEOS-Chem.
922 Measurements from networks other than NOAA were corrected to the NOAA calibration scale, NOAA-
923 2006A, using the results of the WMO Round Robin inter-comparison experiment
924 (https://www.esrl.noaa.gov/gmd/ccgg/wmorr/), where available. For AGAGE and CSIRO, which did not
925 participate in the WMO Round Robins, the data at sites where NOAA discrete samples are also collected
926 were used to calculate a linear regression with NOAA data, which was applied to adjust the data to the

NOAA-2006A scale. For the remaining CSIRO sites where there were no NOAA discrete samples, the mean regression coefficient and offset from all other CSIRO sites were used. The inversions used the discrete sample measurements without averaging, and hourly or daily means of the in-situ measurements, depending on the particular inversion framework.

Each framework applied its own method for calculating the observation space uncertainty, the square of which gives the diagonal elements of the observation error covariance matrix R. The observation space uncertainty accounts for measurement and model representation errors and is equal to the quadratic sum of these terms. Typical values for the observation space uncertainty were between 0.3 and 0.5 ppb for all inversion frameworks.

Prior mean emissions were based on estimates from terrestrial biosphere and ocean biogeochemistry models as well as from inventories. INVICAT, PyVAR-CAMS and GEOS-Chem used the same prior estimates for emissions from natural and agricultural soils from the model OCN v1.1 (*Zaehle et al.*, 2011) and for biomass burning emissions from GFEDv4.1s. For non-soil anthropogenic emissions (namely those from energy, industry and waste sectors), INVICAT, PyVAR-CAMS, and GEOS-Chem used EDGAR v5. MIROC4-ACTM used the VISIT model (*Inatomi et al.*, 2010; *Ito et al.*, 2018) for emissions from natural soils and EDGAR 4.2 for all anthropogenic emissions, including agricultural waste burning, but did not explicitly include a prior estimate for wildfire emissions.

For the prior mean estimate of ocean fluxes, INVICAT, PyVAR-CAMS and GEOS-Chem used the prognostic version of the PlankTOM-v10.2 model (*Buitenhuis et al.*, 2018) with a global total source 2.5 TgN yr^{-1}. Prior uncertainties were estimated in all the inversion frameworks for each grid cell (INVICAT, PyVAR-CAMS and GEOS-Chem) or for each region (MIROC4-ACTM) and the square of these uncertainties formed the diagonal elements of the prior error covariance matrix **B**. INVICAT, PyVAR-CAMS and GEOS-Chem estimated the uncertainty as proportional to the prior value in each grid cell, but MIROC4-ACTM set the uncertainty uniformly for land regions at 1 Tg N yr^{-1} and for ocean regions at 0.5 Tg N yr^{-1}. INVICAT also included off-diagonal covariances in B corresponding to a spatial correlation between flux uncertainties of 500 km and assumed a semi-exponential distribution of uncertainties so as to restrict the possibility of negative fluxes.

S12 Atmospheric N$_2$O Observation Networks

S12.1 The NOAA Network:
For atmospheric N$_2$O observations from the NOAA network (Dutton et al. 2023), we used global mean mixing ratios from the NOAA Global Monitoring Laboratory (GML) (combined dataset based on measurements from five different measurement programs [HATS old flask instrument, HATS current flask instrument (OTTO), the Carbon Cycle and Greenhouse Gases (CCGG) group Cooperative Global Air Sampling Network (https://www.esrl.noaa.gov/gmd/ccgg/flask.php), HATS in situ (RITS program), and HATS in situ (CATS program)]. CCGG provides uncertainties with each measurement (see site files: ftp://aftp.cmdl.noaa.gov/data/greenhouse_gases/n2o/flask/surface/). The CCGG measurements for N$_2$O analysis from more than 50 sites globally was changed to tunable infrared laser direct absorption spectroscopy (TILDAS) in mid-2019 from gas chromatography. About 40 sites of them (mostly Marine Boundary Layer sites) are used to calculate CCGG monthly mean global N$_2$O levels. Monthly mean observations from different NOAA measurement programs are statistically combined to create a long-term NOAA/ESRL GML dataset. Uncertainties (1 sigma) associated with monthly estimates of global mean N$_2$O, are ~1 ppb from 1977−1987, 0.6 ppb from 1988−1994, 0.3−0.4 ppb from 1995−2000, and 0.1 ppb from 2001-2017. NOAA data are generally more consistent after 1995, with standard deviations on the monthly mean mixing ratios at individual sites of ~0.5 ppb from 1995−1998, and 0.1−0.4 ppb after 1998.

977 A detailed description of these measurement programs and the method to combine them are available via
978 https://www.esrl.noaa.gov/gmd/hats/combined/N2O.html.
979
980 **S12.2 The AGAGE network:**
981 The Advanced Global Atmospheric Gases Experiment (AGAGE) global network (and its predecessors ALE
982 and GAGE) (Prinn et al., 2018) has made continuous high-frequency gas chromatographic (GC)
983 measurements with electronic capture detection (ECD) of N_2O at five globally distributed sites since 1978.
984 Improved GC/ECD methods have been deployed over time resulting in N_2O measurement precision of
985 about 0.35% in ALE, 0.13% in GAGE (Prinn et al., 1990) and 0.05% in AGAGE (Prinn et al., 2008; 2018).
986 We used the global mean of AGAGE N_2O measurements during 1980−2020 which are reported on the
987 Scripps Institution of Oceanography SIO-16 scale. Further information on AGAGE stations, instruments,
988 calibration, uncertainties and access to data is available at the AGAGE Data website:
989 https://www.osti.gov/dataexplorer/biblio/dataset/1841748.
990
991 **S12.3 The CSIRO network:**
992 The CSIRO flask network (Francey et al., 2003) consists of nine sampling sites distributed globally and has
993 been in operation since 1992. Flask samples are collected approximately every two weeks and shipped back
994 to CSIRO GASLAB for analysis. Samples were analyzed by gas chromatography with electron capture
995 detection (GC-ECD). One Shimadzu gas chromatograph labelled "Shimadzu-1" (S1) has been used over
996 the entire length of the record and the measurement precision for N_2O from this instrument is about 0.1%.
997 N_2O data from the CSIRO global flask network are reported on the NOAA-2006A N_2O scale and are
998 archived at the World Data Centre for Greenhouse Gases (WDCGG: https://gaw.kishou.go.jp/). Nine sites
999 from the CSIRO network were used to calculate the annual global N_2O mole fractions. Smooth curve fits
1000 to the N_2O data from each of these sites were calculated using the technique outlined in Thoning et al.
1001 (1989), using a short-term cut-off of 80 days. The smooth curve fit data were then placed on an evenly
1002 spaced latitude (5 degree) versus time (weekly) grid using the Kriging interpolation technique. Finally, the
1003 gridded data were used to calculate the global annual values.
1004
1005 **Table S3 Factors used to convert N_2O in various units (by convention Unit 1=Unit 2 × conversion)**

Unit 1	Unit 2	Conversion
Tg N_2O (teragrams of N_2O)	Tg N (teragrams of nitrogen)	1.57
Tg N (teragrams of nitrogen)	g N (grams of nitrogen)	10^{-12}
Tg N (teragrams of nitrogen)	ppb (parts per billion)	4.79

1006

1007 **Table S4 Atmospheric N_2O dry mole fraction measured by different observing networks during 2000-**
1008 **2022.**

ppb	NOAA	AGAGE	CSIRO	Min	Max
2000	315.58	316.18	315.48	315.48	316.18
2001	316.33	316.95	316.12	316.12	316.95
2002	316.99	317.54	316.67	316.67	317.54
2003	317.64	318.26	317.31	317.31	318.26
2004	318.24	318.99	317.99	317.99	318.99

2005	318.98	319.71	318.83	318.83	319.71
2006	319.93	320.39	319.58	319.58	320.39
2007	320.59	321.16	320.34	320.34	321.16
2008	321.54	322.11	321.45	321.45	322.11
2009	322.24	322.91	322.22	322.22	322.91
2010	323.04	323.77	323.08	323.04	323.77
2011	324.21	324.68	324.09	324.09	324.68
2012	325.01	325.65	324.99	324.99	325.65
2013	325.92	326.61	325.89	325.89	326.61
2014	327.06	327.66	326.93	326.93	327.66
2015	328.13	328.52	327.99	327.99	328.52
2016	328.94	329.36	328.77	328.77	329.36
2017	329.75	330.37	329.68	329.68	330.37
2018	330.87	331.53	330.90	330.87	331.53
2019	331.85	332.35	331.66	331.66	332.35
2020	333.06	333.48	332.70	332.70	333.48
2021	334.33	334.81	334.03	334.03	334.81
2022	335.71	336.09	335.57	335.57	336.09

1009

1010 **Table S5: Uncertainty in future projections of atmospheric N_2O dry mole fraction.**

ppb	SSP1-1.9		SSP1-2.6		SSP2-4.5		SSP3-7.0		SSP4-3.4		SSP4-6.0		SSP5-8.5	
Year	Min	Max	Min	Max	Min	Max	Min	Max	Min	Max	Min	Max	Min	Max
2020	330.4	331.1	330.4	331.1	331.0	331.6	331.4	332.0	331.2	331.5	331.2	331.4	331.2	331.9
2030	335.1	336.9	335.5	337.0	337.6	339.6	339.5	342.2	337.5	338.6	338.8	339.6	339.5	341.1
2040	336.2	341.1	336.8	342.0	343.2	347.3	347.9	353.4	340.5	345.7	346.3	349.2	349.2	350.7
2050	336.2	344.6	337.8	345.7	348.5	354.3	356.1	364.9	343.3	353.3	353.5	359.2	359.4	361.2

1011

1012 **References:**

1013

1014 Adalibieke, W., Cui X.Q., Cai H.W., You L.Z., and Zhou F.: Global crop-specific nitrogen fertilization
1015 dataset in 1961-2020, Scientific Data 10, 617, 2023, https://www.nature.com/articles/s41597-023-02526-z

1016 Asaadi, A., and Arora, V. K.: Implementation of nitrogen cycle in the CLASSIC land model,
1017 *Biogeosciences*, *18*(2), 669-706, 2021.

1018 Aumont, O., Éthé, C., Tagliabue, A., Bopp, L., and Gehlen, M.: PISCES-v2: an ocean biogeochemical
1019 model for carbon and ecosystem studies, *Geoscientific Model Development Discussions*, *8*(2), 1375-1509,
1020 2015.

1021   Battaglia, G., and Joos, F.: Marine N2O emissions from nitrification and denitrification constrained by
1022   modern observations and projected in multimillennial global warming simulations, *Global Biogeochemical*
1023   *Cycles*, *32*(1), 92-121, 2018.

1024   Beaulieu, J. J., Tank, J. L., Hamilton, S. K., Wollheim, W. M., Hall Jr, R. O., Mulholland, P. J., Peterson,
1025   B. J., Ashkenas, L. R., Cooper, L. W., and Dahm, C. N. : Nitrous oxide emission from denitrification in
1026   stream and river networks, *Proceedings of the National Academy of Sciences*, *108*(1), 214-219, 2011.

1027   Berdanier, A. B., and Conant, R. T.: Regionally differentiated estimates of cropland N2O emissions reduce
1028   uncertainty in global calculations, *Global Change Biology*, *18*(3), 928-935, 2012.

1029   Berthet, S., Jouanno, J., Séférian, R., Gehlen, M., and Llovel, W.: How does the phytoplankton–light
1030   feedback affect the marine N2O inventory?, *Earth System Dynamics*, *14*(2), 399-412, 2023.

1031   Berthet, S., Séférian, R., Bricaud, C., Chevallier, M., Voldoire, A., and Ethé, C.: Evaluation of an online
1032   grid-coarsening algorithm in a global eddy-admitting ocean biogeochemical model, *Journal of Advances in*
1033   *Modeling Earth Systems*, *11*(6), 1759-1783, 2019.

1034   Bouwman, A. F., Beusen, A. H. W., and Billen, G. : Human alteration of the global nitrogen and phosphorus
1035   soil balances for the period 1970–2050, *Global Biogeochemical Cycles*, *23*(4), 2009.

1036   Bouwman, A. F., Beusen, A. H. W., Overbeek, C. C., Bureau, D. P., Pawlowski, M., and Glibert, P. M.:
1037   Hindcasts and future projections of global inland and coastal nitrogen and phosphorus loads due to finfish
1038   aquaculture, *Reviews in Fisheries Science*, *21*(2), 112-156, 2013.

1039   Bouwman, A. F., Pawłowski, M., Liu, C., Beusen, A. H. W., Shumway, S. E., Glibert, P. M., and Overbeek,
1040   C. C.: Global hindcasts and future projections of coastal nitrogen and phosphorus loads due to shellfish and
1041   seaweed aquaculture, *Reviews in Fisheries Science*, *19*(4), 331-357, 2011.

1042   Buendia, E., Tanabe, K., Kranjc, A., Baasansuren, J., Fukuda, M., Ngarize, S., Osako, A., Pyrozhenko, Y.,
1043   Shermanau, P., and Federici, S.: 2019 Refinement to the 2006 IPCC Guidelines for National Greenhouse
1044   Gas Inventories*Rep.*, 2019.

1045   Buitenhuis, E. T., Suntharalingam, P., and Le Quéré, C.: Constraints on global oceanic emissions of N2O
1046   from observations and models, *Biogeosciences*, *15*(7), 2161-2175, 2018.

1047   Carroll, D., Menemenlis, D., Adkins, J. F., Bowman, K. W., Brix, H., Dutkiewicz, S., Fenty, I., Gierach,
1048   M. M., Hill, C., and Jahn, O.: The ECCO-Darwin data-assimilative global ocean biogeochemistry model:
1049   Estimates of seasonal to multidecadal surface ocean pCO2 and air-sea CO2 flux, *Journal of Advances in*
1050   *Modeling Earth Systems*, *12*(10), e2019MS001888, 2020.

1051   Chatskikh, D., Olesen, J. E., Berntsen, J., Regina, K., and Yamulki, S.: Simulation of effects of soils, climate
1052   and management on N2O emission from grasslands, *Biogeochemistry*, *76*, 395-419, 2005.

1053   Crippa, M., Solazzo, E., Guizzardi, D., Monforti-Ferrario, F., Tubiello, F. N., and Leip, A.: Food systems
1054   are responsible for a third of global anthropogenic GHG emissions, *Nature Food*, *2*(3), 198-209, 2021.

1055   Crippa, M., Solazzo, E., Guizzardi, D., Van Dingenen, R., and Leip, A.: Air pollutant emissions from global
1056   food systems are responsible for environmental impacts, crop losses and mortality, *Nature Food*, 1-15,
1057   2022.

1058   Cui, X., Zhou, F., Ciais, P., Davidson, E. A., Tubiello, F. N., Niu, X., Ju, X., Canadell, J. G., Bouwman, A.
1059   F., and Jackson, R. B.: Global mapping of crop-specific emission factors highlights hotspots of nitrous
1060   oxide mitigation, *Nature Food*, *2*(11), 886-893, 2021.

1061   Davidson, E. A., de Carvalho, C. J. R., Figueira, A. M., Ishida, F. Y., Ometto, J. P. H. B., Nardoto, G. B.,
1062   Sabá, R. T., Hayashi, S. N., Leal, E. C., and Vieira, I. C. G.: Recuperation of nitrogen cycling in Amazonian
1063   forests following agricultural abandonment, *Nature*, *447*(7147), 995-998, 2007.

Davidson, E. A., Keller, M., Erickson, H. E., Verchot, L. V., and Veldkamp, E.: Testing a conceptual model of soil emissions of nitrous and nitric oxides: using two functions based on soil nitrogen availability and soil water content, the hole-in-the-pipe model characterizes a large fraction of the observed variation of nitric oxide and nitrous oxide emissions from soils, *Bioscience*, *50*(8), 667-680, 2000.

Decock, C.: Mitigating nitrous oxide emissions from corn cropping systems in the midwestern US: Potential and data gaps, *Environmental Science & Technology*, *48*(8), 4247-4256, 2014.

Deemer, B. R., Harrison, J. A., Li, S., Beaulieu, J. J., DelSontro, T., Barros, N., Bezerra-Neto, J. F., Powers, S. M., Dos Santos, M. A., and Vonk, J. A.: Greenhouse gas emissions from reservoir water surfaces: a new global synthesis, *BioScience*, *66*(11), 949-964, 2016.

Del Grosso, S. J., Parton, W. J., Mosier, A. R., Ojima, D. S., Kulmala, A. E., and Phongpan, S.: General model for N2O and N2 gas emissions from soils due to dentrification, *Global biogeochemical cycles*, *14*(4), 1045-1060, 2000.

Döll, P., and Lehner, B.: Validation of a new global 30-min drainage direction map, *Journal of Hydrology*, *258*(1-4), 214-231, 2002.

Dürr, H. H., Laruelle, G. G., van Kempen, C. M., Slomp, C. P., Meybeck, M., and Middelkoop, H.: Worldwide typology of nearshore coastal systems: defining the estuarine filter of river inputs to the oceans, *Estuaries Coasts*, *34*, 441-458, 2011.

Eggleston, H. S., Buendia, L., Miwa, K., Ngara, T., and Tanabe, K. : 2006 IPCC guidelines for national greenhouse gas inventories, 2006.

FAO (2020), FAO Fisheries and Aquaculture - FishStatJ - Software for Fishery and Aquaculture Statistical Time Series. In: FAO Fisheries and Aquaculture Division [online]. Rome. [Cited 3 November 2021]. , edited.

FAO (2022), FAOSTAT Climate Change, Emissions, Emissions Totals, edited.

Ganesan, A. L., Manizza, M., Morgan, E. J., Harth, C. M., Kozlova, E., Lueker, T., Manning, A. J., Lunt, M. F., Mühle, J., and Lavric, J. V.: Marine nitrous oxide emissions from three Eastern Boundary Upwelling Systems inferred from atmospheric observations, *Geophysical Research Letters*, *47*(14), e2020GL087822, 2020.

Goldewijk, K. K., Beusen, A., Doelman, J., and Stehfest, E.: Anthropogenic land use estimates for the Holocene–HYDE 3.2, *Earth System Science Data*, *9*(2), 927-953, 2017.

Hall, B. D., Dutton, G. S., and Elkins, J. W.: The NOAA nitrous oxide standard scale for atmospheric observations, *Journal of Geophysical Research: Atmospheres*, *112*(D9), 2007.

Harris, I. P. D. J., Jones, P. D., Osborn, T. J., and Lister, D. H.: Updated high-resolution grids of monthly climatic observations–the CRU TS3. 10 Dataset, *International journal of climatology*, *34*(3), 623-642, 2014.

Heinen, M.: Simplified denitrification models: overview and properties, *Geoderma*, *133*(3-4), 444-463, 2006.

Helgason, B. L., Janzen, H. H., Chantigny, M. H., Drury, C. F., Ellert, B. H., Gregorich, E. G., Lemke, R. L., Pattey, E., Rochette, P., and Wagner-Riddle, C.: Toward improved coefficients for predicting direct N2O emissions from soil in Canadian agroecosystems, *Nutrient Cycling in Agroecosystems*, *72*, 87-99, 2005.

Hénault, C., Bizouard, F., Laville, P., Gabrielle, B., Nicoullaud, B., Germon, J. C., and Cellier, P.: Predicting in situ soil N2O emission using NOE algorithm and soil database, *Global Change Biology*, *11*(1), 115-127, 2005.

1107 Hersbach, H., Bell, B., Berrisford, P., Hirahara, S., Horányi, A., Muñoz-Sabater, J., Nicolas, J., Peubey, C.,
1108 Radu, R., and Schepers, D.: Complete ERA5 from 1979: Fifth generation of ECMWF atmospheric
1109 reanalyses of the global climate, *Copernicus Climate Change Service Data Store*, 2017.

1110 Hickman, J. E., Scholes, R. J., Rosenstock, T. S., Garcia-Pando, C. P., and Nyamangara, J.: Assessing non-
1111 CO2 climate-forcing emissions and mitigation in sub-Saharan Africa, *Current Opinion in Environmental*
1112 *Sustainability*, *9*, 65-72, 2014.

1113 Hu, M., Chen, D., and Dahlgren, R. A.: Modeling nitrous oxide emission from rivers: a global assessment,
1114 *Global Change Biology*, *22*(11), 3566-3582, 2016.

1115 Huang, Y., and Gerber, S.: Global soil nitrous oxide emissions in a dynamic carbon-nitrogen model,
1116 *Biogeosciences*, *12*(21), 6405-6427, 2015.

1117 Hurtt, G. C., Chini, L., Sahajpal, R., Frolking, S., Bodirsky, B. L., Calvin, K., Doelman, J. C., Fisk, J.,
1118 Fujimori, S., and Klein Goldewijk, K.: Harmonization of global land use change and management for the
1119 period 850–2100 (LUH2) for CMIP6, *Geoscientific Model Development*, *13*(11), 5425-5464, 2020.

1120 IEA: World Energy Outlook 2021*Rep.*, IEA, Paris, 2021.

1121 Inatomi, M., Ito, A., Ishijima, K., and Murayama, S.: Greenhouse gas budget of a cool-temperate deciduous
1122 broad-leaved forest in Japan estimated using a process-based model, *Ecosystems*, *13*, 472-483, 2010.

1123 IPCC: Revised 1996 IPCC Guidelines for National Greenhouse Gas Inventories, 1996.

1124 IPCC: Good practice guidance and uncertainty management in national greenhouse gas inventories, 2000.

1125 IPCC: IPCC Guidelines for National Greenhouse Gas Inventories*Rep.*, Hayama, Japan, 2006.

1126 Ito, A., Nishina, K., Ishijima, K., Hashimoto, S., and Inatomi, M.: Emissions of nitrous oxide (N 2 O) from
1127 soil surfaces and their historical changes in East Asia: a model-based assessment, *Progress in Earth*
1128 *Planetary Science*, *5*, 1-13, 2018.

1129 Janssens-Maenhout, G., Crippa, M., Guizzardi, D., Muntean, M., Schaaf, E., Dentener, F., Bergamaschi,
1130 P., Pagliari, V., Olivier, J. G., and Peters, J. A.: EDGAR v4. 3.2 Global Atlas of the three major greenhouse
1131 gas emissions for the period 1970–2012, *Earth System Science Data*, *11*(3), 959-1002, 2019.

1132 Jin, X., and Gruber, N.: Offsetting the radiative benefit of ocean iron fertilization by enhancing N2O
1133 emissions, *Geophysical research letters*, *30*(24), 2003.

1134 Johnson, D. J., Niedbalski, N. P., Ervin, J. S., and Patnaik, S. S.: Ammonium carbamate-based heat
1135 exchanger reactor as an endothermic heat sink for thermal management, *International Journal of Heat Mass*
1136 *Transfer*, *91*, 766-776, 2015.

1137 Kalnay, E., Kanamitsu, M., Kistler, R., Collins, W., Deaven, D., Gandin, L., Iredell, M., Saha, S., White,
1138 G., and Woollen, J.: The NCEP/NCAR 40-year reanalysis project, *Bulletin of the American meteorological*
1139 *Society*, *77*(3), 437-472, 1996.

1140 Keller, M., and Reiners, W. A.: Soil-atmosphere exchange of nitrous oxide, nitric oxide, and methane under
1141 secondary succession of pasture to forest in the Atlantic lowlands of Costa Rica, *Global Biogeochemical*
1142 *Cycles*, *8*(4), 399-409, 1994.

1143 Kim, D.-G., Giltrap, D., and Hernandez-Ramirez, G.: Background nitrous oxide emissions in agricultural
1144 and natural lands: a meta-analysis, *Plant Soil*, *373*, 17-30, 2013a.

1145 Kim, D.-G., Hernandez-Ramirez, G., and Giltrap, D.: Linear and nonlinear dependency of direct nitrous
1146 oxide emissions on fertilizer nitrogen input: A meta-analysis, *Agriculture, Ecosystems Environment*, *168*,
1147 53-65, 2013b.

Kock, A., and Bange, H. W.: Counting the ocean's greenhouse gas emissions, *Eos: Earth Space Science News*, *96*(3), 10-13, 2015.

Kou Giesbrecht, S., and Arora, V. K.: Representing the dynamic response of vegetation to nitrogen limitation via biological nitrogen fixation in the CLASSIC Land Model, *Global Biogeochemical Cycles*, *36*(6), e2022GB007341, 2022.

Landolfi, A., Somes, C. J., Koeve, W., Zamora, L. M., and Oschlies, A.: Oceanic nitrogen cycling and N2O flux perturbations in the Anthropocene, *Global Biogeochemical Cycles*, *31*(8), 1236-1255, 2017.

Laruelle, G. G., Landschützer, P., Gruber, N., Tison, J.-L., Delille, B., and Regnier, P.: Global high-resolution monthly pCO2 climatology for the coastal ocean derived from neural network interpolation, *Biogeosciences*, *14*(19), 4545-4561, 2017.

Lauerwald, R., Regnier, P., Figueiredo, V., Enrich-Prast, A., Bastviken, D., Lehner, B., Maavara, T., and Raymond, P.: Natural lakes are a minor global source of N2O to the atmosphere, *Global Biogeochemical Cycles*, *33*(12), 1564-1581, 2019.

Le Quéré, C., Buitenhuis, E. T., Moriarty, R., Alvain, S., Aumont, O., Bopp, L., Chollet, S., Enright, C., Franklin, D. J., and Geider, R. J.: Role of zooplankton dynamics for Southern Ocean phytoplankton biomass and global biogeochemical cycles, *Biogeosciences*, *13*(14), 4111-4133, 2016.

Lehner, B., Liermann, C. R., Revenga, C., Vörösmarty, C., Fekete, B., Crouzet, P., Döll, P., Endejan, M., Frenken, K., and Magome, J. : High-resolution mapping of the world's reservoirs and dams for sustainable river-flow management, *Frontiers in Ecology the Environment*, *9*(9), 494-502, 2011.

Lehner, B., Verdin, K., and Jarvis, A.: New global hydrography derived from spaceborne elevation data, *Eos, Transactions American Geophysical Union*, *89*(10), 93-94, 2008.

Lehuger, S., Gabrielle, B., Laville, P., Lamboni, M., Loubet, B., and Cellier, P.: Predicting and mitigating the net greenhouse gas emissions of crop rotations in Western Europe, *Agricultural Forest Meteorology*, *151*(12), 1654-1671, 2011.

Leppelt, T., Dechow, R., Gebbert, S., Freibauer, A., Lohila, A., Augustin, J., Drösler, M., Fiedler, S., Glatzel, S., and Höper, H.: Nitrous oxide emission budgets and land-use-driven hotspots for organic soils in Europe, *Biogeosciences*, *11*(23), 6595-6612, 2014.

Lan, X., E.J. Dlugokencky, J.W. Mund, A.M. Crotwell, M.J. Crotwell, E. Moglia, M. Madronich, D. Neff and K.W. Thoning (2022), Atmospheric Nitrous Oxide Dry Air Mole Fractions from the NOAA GML Carbon Cycle Cooperative Global Air Sampling Network, 1997-2021, Version: 2022-11-21, https://doi.org/10.15138/53g1-x417

Li, C., Aber, J., Stange, F., Butterbach-Bahl, K., and Papen, H.: A process-oriented model of N2O and NO emissions from forest soils: 1. Model development, *Journal of Geophysical Research: Atmospheres*, *105*(D4), 4369-4384, 2000.

Li, C., Frolking, S., and Frolking, T. A.: A model of nitrous oxide evolution from soil driven by rainfall events: 2. Model applications, *Journal of Geophysical Research: Atmospheres*, *97*(D9), 9777-9783, 1992.

Liang, J. H., Deutsch, C., McWilliams, J. C., Baschek, B., Sullivan, P. P., and Chiba, D.: Parameterizing bubble-mediated air-sea gas exchange and its effect on ocean ventilation, *Global Biogeochemical Cycles*, *27*(3), 894-905, 2013.

Lu, C., and Tian, H.: Net greenhouse gas balance in response to nitrogen enrichment: perspectives from a coupled biogeochemical model, *Global Change Biology*, *19*(2), 571-588, 2013.

Maavara, T., Lauerwald, R., Laruelle, G. G., Akbarzadeh, Z., Bouskill, N. J., Van Cappellen, P., and Regnier, P.: Nitrous oxide emissions from inland waters: Are IPCC estimates too high?, *Global Change Biology*, *25*(2), 473-488, 2019.

1192 Madec, G.: NEMO ocean engine: Note du pole de modélisation, Institut Pierre-Simon Laplace (IPSL),
1193 France, No 27 ISSN No 1288-1619, *France: IPSL*, 2008.

1194 Madec, G., Bourdallé-Badie, R., Bouttier, P.-A., Bricaud, C., Bruciaferri, D., Calvert, D., Chanut, J.,
1195 Clementi, E., Coward, A., and Delrosso, D.: NEMO ocean engine, 2017.

1196 Manizza, M., Menemenlis, D., Zhang, H., and Miller, C. E.: Modeling the recent changes in the Arctic
1197 Ocean CO2 sink (2006–2013), *Global Biogeochemical Cycles*, *33*(3), 420-438, 2019.

1198 Manizza, M., Carroll, D., Menemenlis, D., Zhang, H., & Miller, C. E.: Modeling the recent changes of
1199 phytoplankton blooms dynamics in the Arctic Ocean. Journal of Geophysical Research: Oceans, 128,
1200 e2022JC019152, 2023.

1201 Martinez-Rey, J., Bopp, L., Gehlen, M., Tagliabue, A., and Gruber, N.: Projections of oceanic N2O
1202 emissions in the 21st century using the IPSL Earth system model, *Biogeosciences*, *12*(13), 4133-4148, 2015.

1203 Marzadri, A., Amatulli, G., Tonina, D., Bellin, A., Shen, L. Q., Allen, G. H., and Raymond, P. A.: Global
1204 riverine nitrous oxide emissions: The role of small streams and large rivers, *Science of The Total
1205 Environment*, *776*, 145148, 2021.

1206 Marzadri, A., Dee, M. M., Tonina, D., Bellin, A., and Tank, J. L.: Role of surface and subsurface processes
1207 in scaling N2O emissions along riverine networks, *Proceedings of the National Academy of Sciences*,
1208 *114*(17), 4330-4335, 2017.

1209 McCrackin, M. L., Harrison, J. A., and Compton, J. E.: Factors influencing export of dissolved inorganic
1210 nitrogen by major rivers: A new, seasonal, spatially explicit, global model, *Global Biogeochemical Cycles*,
1211 *28*(3), 269-285, 2014.

1212 Melillo, J. M., Steudler, P. A., Feigl, B. J., Neill, C., Garcia, D., Piccolo, M. C., Cerri, C. C., and Tian, H.:
1213 Nitrous oxide emissions from forests and pastures of various ages in the Brazilian Amazon, *Journal of
1214 Geophysical Research: Atmospheres*, *106*(D24), 34179-34188, 2001.

1215 Messager, M. L., Lehner, B., Grill, G., Nedeva, I., and Schmitt, O.: Estimating the volume and age of water
1216 stored in global lakes using a geo-statistical approach, *Nature Communications*, *7*(1), 13603, 2016.

1217 Nevison, C., Butler, J. H., and Elkins, J. W.: Global distribution of N2O and the ΔN2O-AOU yield in the
1218 subsurface ocean, *Global Biogeochemical Cycles*, *17*(4), 2003.

1219 Pan, S., Bian, Z., Tian, H., Yao, Y., Najjar, R. G., Friedrichs, M. A. M., Hofmann, E. E., Xu, R., and Zhang,
1220 B.: Impacts of multiple environmental changes on long-term nitrogen loading from the Chesapeake Bay
1221 watershed, *Journal of Geophysical Research: Biogeosciences*, *126*(5), e2020JG005826, 2021.

1222 Parekh, P., Joos, F., and Müller, S. A.: A modeling assessment of the interplay between aeolian iron fluxes
1223 and iron-binding ligands in controlling carbon dioxide fluctuations during Antarctic warm events,
1224 *Paleoceanography*, *23*(4), 2008.

1225 Parton, W. J., Mosier, A. R., Ojima, D. S., Valentine, D. W., Schimel, D. S., Weier, K., and Kulmala, A.
1226 E.: Generalized model for N2 and N2O production from nitrification and denitrification, *Global
1227 biogeochemical cycles*, *10*(3), 401-412, 1996.

1228 Patra, P. K., Dlugokencky, E. J., Elkins, J. W., Dutton, G. S., Tohjima, Y., Sasakawa, M., Ito, A., Weiss,
1229 R. F., Manizza, M., and Krummel, P. B.: Forward and inverse modelling of atmospheric nitrous oxide using
1230 MIROC4-atmospheric chemistry-transport model, *Journal of the Meteorological Society of Japan. Ser. II*,
1231 *100*(2), 361-386, 2022.

1232 Patra, P. K., Takigawa, M., Watanabe, S., Chandra, N., Ishijima, K., and Yamashita, Y.: Improved chemical
1233 tracer simulation by MIROC4. 0-based atmospheric chemistry-transport model (MIROC4-ACTM), *Sola*,
1234 *14*, 91-96, 2018.

1235   Paulot, F., Jacob, D. J., Johnson, M. T., Bell, T. G., Baker, A. R., Keene, W. C., Lima, I. D., Doney, S. C.,
1236   and Stock, C. A.: Global oceanic emission of ammonia: Constraints from seawater and atmospheric
1237   observations, *Global Biogeochemical Cycles*, *29*(8), 1165-1178, 2015.

1238   Peltier, W. R.: Global glacial isostasy and the surface of the ice-age Earth: the ICE-5G (VM2) model and
1239   GRACE, *Annual Review of Earth and Planetary Sciences*, *32*, 111-149, 2004.

1240   Portmann, F. T., Siebert, S., and Döll, P.: MIRCA2000—Global monthly irrigated and rainfed crop areas
1241   around the year 2000: A new high-resolution data set for agricultural and hydrological modeling, *Global*
1242   *Biogeochemical Cycles*, *24*(1), 2010.

1243   Porwollik, V., Rolinski, S., Heinke, J., and Müller, C.: Generating a rule-based global gridded tillage
1244   dataset, *Earth System Science Data*, *11*(2), 823-843, 2019.

1245   Prather, M. J., Hsu, J., DeLuca, N. M., Jackman, C. H., Oman, L. D., Douglass, A. R., Fleming, E. L.,
1246   Strahan, S. E., Steenrod, S. D., and Søvde, O. A.: Measuring and modeling the lifetime of nitrous oxide
1247   including its variability, *Journal of Geophysical Research: Atmospheres*, *120*(11), 5693-5705, 2015.

1248   Resplandy, L., Hogikyan, A., Müller, J. D., Najjar, R. G., Bange, H. W., Bianchi, D., et al.: A synthesis of
1249   global coastal ocean greenhouse gas fluxes. Global Biogeochemical Cycles, 38, e2023GB007803, 2024.

1250   Rochette, P., and Janzen, H. H.: Towards a revised coefficient for estimating N2O emissions from legumes,
1251   *Nutrient Cycling in Agroecosystems*, *73*, 171-179, 2005.

1252   Rosentreter, J. A., Laruelle, G. G., Bange, H. W., Bianchi, T. S., Busecke, J. J. M., Cai, W.-J., Eyre, B. D.,
1253   Forbrich, I., Kwon, E. Y., and Maavara, T.: Coastal vegetation and estuaries are collectively a greenhouse
1254   gas sink, *Nature Climate Change*, 1-9, 2023.

1255   Sacks, W. J., Deryng, D., Foley, J. A., and Ramankutty, N.: Crop planting dates: an analysis of global
1256   patterns, *Global Ecology Biogeography*, *19*(5), 607-620, 2010.

1257   Salas y Mélia, D.: A global coupled sea ice–ocean model, *Ocean Modelling*, *4*(2), 137-172, 2002.

1258   Séférian, R., Nabat, P., Michou, M., Saint-Martin, D., Voldoire, A., Colin, J., Decharme, B., Delire, C.,
1259   Berthet, S., and Chevallier, M.: Evaluation of CNRM Earth System Model, CNRM-ESM2-1: role of Earth
1260   system processes in present-day and future climate, *Journal of Advances in Modeling Earth Systems*,
1261   *11*(12), 4182-4227, 2019.

1262   Shangguan, W., Dai, Y., Duan, Q., Liu, B., and Yuan, H.: A global soil data set for earth system modeling,
1263   *Journal of Advances in Modeling Earth Systems*, *6*(1), 249-263, 2014.

1264   Shcherbak, I., Millar, N., and Robertson, G. P.: Global metaanalysis of the nonlinear response of soil nitrous
1265   oxide (N2O) emissions to fertilizer nitrogen, *Proceedings of the National Academy of Sciences*, *111*(25),
1266   9199-9204, 2014.

1267   Shu, S., Jain, A. K., Koven, C. D., and Mishra, U.: Estimation of permafrost SOC stock and turnover time
1268   using a land surface model with vertical heterogeneity of permafrost soils, *Global Biogeochemical Cycles*,
1269   *34*(11), e2020GB006585, 2020.

1270   Solazzo, E., Crippa, M., Guizzardi, D., Muntean, M., Choulga, M., and Janssens-Maenhout, G.:
1271   Uncertainties in the Emissions Database for Global Atmospheric Research (EDGAR) emission inventory
1272   of greenhouse gases, *Atmospheric Chemistry Physics*, *21*(7), 5655-5683, 2021.

1273   Stehfest, E., and Bouwman, L.: N2O and NO emission from agricultural fields and soils under natural
1274   vegetation: summarizing available measurement data and modeling of global annual emissions, *Nutrient*
1275   *cycling in agroecosystems*, *74*, 207-228, 2006.

Sullivan, B. W., Nifong, R. L., Nasto, M. K., Alvarez-Clare, S., Dencker, C. M., Soper, F. M., Shoemaker, K. T., Ishida, F. Y., Zaragoza-Castells, J., and Davidson, E. A.: Biogeochemical recuperation of lowland tropical forest during succession, *Ecology*, *100*(4), e02641, 2019.

Tarantola, A.: *Inverse problem theory and methods for model parameter estimation*, SIAM, 2005.

Thompson, R. L., Chevallier, F., Crotwell, A. M., Dutton, G., Langenfelds, R. L., Prinn, R. G., Weiss, R. F., Tohjima, Y., Nakazawa, T., and Krummel, P. B.: Nitrous oxide emissions 1999 to 2009 from a global atmospheric inversion, *Atmospheric Chemistry Physics*, *14*(4), 1801-1817, 2014.

Thornton, P. E., and Rosenbloom, N. A.: Ecosystem model spin-up: Estimating steady state conditions in a coupled terrestrial carbon and nitrogen cycle model, *Ecological Modelling*, *189*(1-2), 25-48, 2005.

Tian, H., Bian, Z., Shi, H., Qin, X., Pan, N., Lu, C., Pan, S., Tubiello, F. N., Chang, J., and Conchedda, G.: History of anthropogenic Nitrogen inputs (HaNi) to the terrestrial biosphere: a 5 arcmin resolution annual dataset from 1860 to 2019, *Earth System Science Data*, *14*(10), 4551-4568, 2022.

Tian, H., Chen, G., Zhang, C., Liu, M., Sun, G., Chappelka, A., Ren, W., Xu, X., Lu, C., and Pan, S.: Century-scale responses of ecosystem carbon storage and flux to multiple environmental changes in the southern United States, *Ecosystems*, *15*, 674-694, 2012a.

Tian, H., Lu, C., Chen, G., Tao, B., Pan, S., Grosso, S. J. D., Xu, X., Bruhwiler, L., Wofsy, S. C., and Kort, E. A.: Contemporary and projected biogenic fluxes of methane and nitrous oxide in North American terrestrial ecosystems, *Frontiers in Ecology the Environment*, *10*(10), 528-536, 2012b.

Tian, H., Ren, W., Yang, J., Tao, B., Cai, W. J., Lohrenz, S. E., Hopkinson, C. S., Liu, M., Yang, Q., and Lu, C.: Climate extremes dominating seasonal and interannual variations in carbon export from the Mississippi River Basin, *Global Biogeochemical Cycles*, *29*(9), 1333-1347, 2015.

Tian, H., Xu, R., Canadell, J. G., Thompson, R. L., Winiwarter, W., Suntharalingam, P., Davidson, E. A., Ciais, P., Jackson, R. B., Janssens-Maenhout, G., ..., and Yuanzhi, Y.: A comprehensive quantification of global nitrous oxide sources and sinks, *Nature*, *586*(7828), 248-256, 2020a.

Tian, H., Xu, R., Pan, S., Yao, Y., Bian, Z., Cai, W. J., Hopkinson, C. S., Justic, D., Lohrenz, S., and Lu, C.: Long-term trajectory of nitrogen loading and delivery from Mississippi River Basin to the Gulf of Mexico, *Global Biogeochemical Cycles*, *34*(5), e2019GB006475, 2020b.

Tian, H., Xu, X., Liu, M., Ren, W., Zhang, C., Chen, G., and Lu, C.: Spatial and temporal patterns of CH_4 and N_2O fluxes in terrestrial ecosystems of North America during 1979–2008: application of a global biogeochemistry model, *Biogeosciences*, *7*(9), 2673-2694, 2010.

Tian, H., Xu, X., Lu, C., Liu, M., Ren, W., Chen, G., Melillo, J., and Liu, J.: Net exchanges of CO_2, CH_4, and N_2O between China's terrestrial ecosystems and the atmosphere and their contributions to global climate warming, *Journal of Geophysical Research: Biogeosciences*, *116*(G2), 2011.

Tian, H., Yang, J., Lu, C., Xu, R., Canadell, J. G., Jackson, R. B., Arneth, A., Chang, J., Chen, G., and Ciais, P.: The global N2O model intercomparison project, *Bulletin of the American Meteorological Society*, *99*(6), 1231-1251, 2018.

Tian, H., R. Xu, S. Pan, Y. Yao, Z. Bian, W. J. Cai, C. S. Hopkinson, D. Justic, S. Lohrenz, C. Lu, W. Ren, and J. Yang. (2020). Long-Term Trajectory of Nitrogen Loading and Delivery From Mississippi River Basin to the Gulf of Mexico. *Global Biogeochemical Cycles*, *34*(5), e2019GB006475. https://doi.org/10.1029/2019GB006475.

Tschumi, T., Joos, F., Gehlen, M., and Heinze, C.: Deep ocean ventilation, carbon isotopes, marine sedimentation and the deglacial CO_2 rise, *Climate of the Past*, *7*(3), 771-800, 2011.

Tsujino, H., Urakawa, L. S., Griffies, S. M., Danabasoglu, G., Adcroft, A. J., Amaral, A. E., Arsouze, T., Bentsen, M., Bernardello, R., and Böning, C. W.: Evaluation of global ocean–sea-ice model simulations

1320 based on the experimental protocols of the Ocean Model Intercomparison Project phase 2 (OMIP-2),
1321 *Geoscientific Model Development*, *13*(8), 3643-3708, 2020.

1322 Tsujino, H., Urakawa, S., Nakano, H., Small, R. J., Kim, W. M., Yeager, S. G., Danabasoglu, G., Suzuki,
1323 T., Bamber, J. L., and Bentsen, M.: JRA-55 based surface dataset for driving ocean–sea-ice models (JRA55-
1324 do), *Ocean Modelling*, *130*, 79-139, 2018.

1325 Van Drecht, G., Bouwman, A. F., Harrison, J., and Knoop, J. M.: Global nitrogen and phosphate in urban
1326 wastewater for the period 1970 to 2050, *Global Biogeochemical Cycles*, *23*(4), 2009.

1327 Van Drecht, G., Bouwman, A. F., Knoop, J. M., Beusen, A. H. W., and Meinardi, C. R.: Global modeling
1328 of the fate of nitrogen from point and nonpoint sources in soils, groundwater, and surface water, *Global
1329 Biogeochemical Cycles*, *17*(4), 2003.

1330 Verchot, L. V., Davidson, E. A., Cattânio, H., Ackerman, I. L., Erickson, H. E., and Keller, M.: Land use
1331 change and biogeochemical controls of nitrogen oxide emissions from soils in eastern Amazonia, *Global
1332 Biogeochemical Cycles*, *13*(1), 31-46, 1999.

1333 Walter, K., Don, A., Fuß, R., Kern, J., Drewer, J., and Flessa, H.: Direct nitrous oxide emissions from
1334 oilseed rape cropping–a meta-analysis, *Gcb Bioenergy*, *7*(6), 1260-1271, 2015.

1335 Wang, Q., Zhou, F., Shang, Z., Ciais, P., Winiwarter, W., Jackson, R. B., Tubiello, F. N., Janssens-
1336 Maenhout, G., Tian, H., and Cui, X.: Data-driven estimates of global nitrous oxide emissions from
1337 croplands, *National Science Review*, *7*(2), 441–452, 2020.

1338 Wanninkhof, R.: Relationship between wind speed and gas exchange over the ocean, *Journal of
1339 Geophysical Research: Oceans*, *97*(C5), 7373-7382, 1992.

1340 Wanninkhof, R.: Relationship between wind speed and gas exchange over the ocean revisited, *Limnology
1341 Oceanography: Methods*, *12*(6), 351-362, 2014.

1342 Weiss, R. F., and Price, B. A.: Nitrous oxide solubility in water and seawater, *Marine Chemistry*, *8*(4), 347-
1343 359, 1980.

1344 Wells, K. C., Millet, D. B., Bousserez, N., Henze, D. K., Chaliyakunnel, S., Griffis, T. J., Luan, Y.,
1345 Dlugokencky, E. J., Prinn, R. G., and O'Doherty, S.: Simulation of atmospheric N 2 O with GEOS-Chem
1346 and its adjoint: evaluation of observational constraints, *Geoscientific Model Development*, *8*(10), 3179-
1347 3198, 2015.

1348 Wilson, C., Chipperfield, M. P., Gloor, M., and Chevallier, F.: Development of a variational flux inversion
1349 system (INVICAT v1. 0) using the TOMCAT chemical transport model, *Geoscientific Model Development*,
1350 *7*(5), 2485-2500, 2014.

1351 Wollheim, W. M., Vörösmarty, C. J., Bouwman, A. F., Green, P., Harrison, J., Linder, E., Peterson, B. J.,
1352 Seitzinger, S. P., and Syvitski, J. P. M.: Global N removal by freshwater aquatic systems using a spatially
1353 distributed, within-basin approach, *Global Biogeochemical Cycles*, *22*(2), 2008.

1354 Xu-Ri, and Prentice, I. C.: Terrestrial nitrogen cycle simulation with a dynamic global vegetation model,
1355 *Global Change Biology*, *14*(8), 1745-1764, 2008.

1356 Xu, R., Tian, H., Lu, C., Pan, S., Chen, J., Yang, J., and Zhang, B.: Preindustrial nitrous oxide emissions
1357 from the land biosphere estimated by using a global biogeochemistry model, *Climate of the Past*, *13*(7),
1358 977-990, 2017.

1359 Xu, X., Sharma, P., Shu, S., Lin, T.-S., Ciais, P., Tubiello, F. N., Smith, P., Campbell, N., and Jain, A. K.:
1360 Global greenhouse gas emissions from animal-based foods are twice those of plant-based foods, *Nature
1361 Food*, *2*(9), 724-732, 2021.

Xu, X., Tian, H., Liu, M., Ren, W., Chen, G., Lu, C., and Zhang, C.: Multiple-factor controls on terrestrial N2O flux over North America from 1979 through 2010, *Biogeosciences Discussions*, *8*(6), 2011.

Yang, H., Zhou, F., Piao, S., Huang, M., Chen, A., Ciais, P., Li, Y., Lian, X., Peng, S., and Zeng, Z.: Regional patterns of future runoff changes from Earth system models constrained by observation, *Geophysical Research Letters*, *44*(11), 5540-5549, 2017.

Yang, Q., Tian, H., Friedrichs, M. A. M., Hopkinson, C. S., Lu, C., and Najjar, R. G.: Increased nitrogen export from eastern North America to the Atlantic Ocean due to climatic and anthropogenic changes during 1901–2008, *Journal of Geophysical Research: Biogeosciences*, *120*(6), 1046-1068, 2015.

Yang, S., Chang, B. X., Warner, M. J., Weber, T. S., Bourbonnais, A. M., Santoro, A. E., Kock, A., Sonnerup, R. E., Bullister, J. L., and Wilson, S. T.: Global reconstruction reduces the uncertainty of oceanic nitrous oxide emissions and reveals a vigorous seasonal cycle, *Proceedings of the National Academy of Sciences*, *117*(22), 11954-11960, 2020.

Yang, X., Wittig, V., Jain, A. K., and Post, W.: Integration of nitrogen cycle dynamics into the Integrated Science Assessment Model for the study of terrestrial ecosystem responses to global change, *Global Biogeochemical Cycles*, *23*(4), 2009.

Yao, Y., Tian, H., Shi, H., Pan, S., Xu, R., Pan, N., and Canadell, J. G.: Increased global nitrous oxide emissions from streams and rivers in the Anthropocene, *Nature Climate Change*, *10*(2), 138-142, 2020.

Yao, Y., Tian, H., Xu, X., Li, Y., and Pan, S.: Dynamics and controls of inland water CH4 emissions across the Conterminous United States: 1860-2019, *Water Research*, *224*, 119043, 2022.

Yool, A., Martin, A. P., Fernández, C., and Clark, D. R.: The significance of nitrification for oceanic new production, *Nature*, *447*(7147), 999-1002, 2007.

Zaehle, S., Ciais, P., Friend, A. D., and Prieur, V.: Carbon benefits of anthropogenic reactive nitrogen offset by nitrous oxide emissions, *Nature Geoscience*, *4*(9), 601-605, 2011.

Zaehle, S., and Friend, A. D.: Carbon and nitrogen cycle dynamics in the O-CN land surface model: 1. Model description, site-scale evaluation, and sensitivity to parameter estimates, *Global Biogeochemical Cycles*, *24*(1), 2010.

Zamora, L. M., and Oschlies, A.: Surface nitrification: A major uncertainty in marine N2O emissions, *Geophysical Research Letters*, *41*(12), 4247-4253, 2014.

Zhang, Y., Li, C., Zhou, X., and Moore III, B.: A simulation model linking crop growth and soil biogeochemistry for sustainable agriculture, *Ecological Modelling*, *151*(1), 75-108, 2002.

Zhou, F., Shang, Z., Zeng, Z., Piao, S., Ciais, P., Raymond, P. A., Wang, X., Wang, R., Chen, M., and Yang, C.: New model for capturing the variations of fertilizer-induced emission factors of N2O, *Global Biogeochemical Cycles*, *29*(6), 885-897, 2015.

Zhou, J. B., Jiang, M. M., and Chen, G. Q.: Estimation of methane and nitrous oxide emission from livestock and poultry in China during 1949–2003, *Energy Policy*, *35*(7), 3759-3767, 2007.

Zhu, Q., Riley, W. J., Tang, J., and Koven, C. D. : Multiple soil nutrient competition between plants, microbes, and mineral surfaces: model development, parameterization, and example applications in several tropical forests, *Biogeosciences*, *13*(1), 341-363, 2016.